Gondwana Research 142 (2025) 236–251

Contents lists available at ScienceDirect

Gondwana Research

journal homepage: www.elsevier.com/locate/gr

A vertical reverse zoning in the Kunshan W-Mo-Cu deposit, South China: Insights from mineral paragenesis, zircon geochemistry and S-Pb-O isotopes

Qingqing Yin [a,b], Juxing Tang [a,b], Qiuming Pei [a,*], Inna Safonova [a,c], Xinkui Xiang [d], Jingjing Dai [b], Aorigele Zhou [b], Bin Lin [b,e], Yumin Xu [d], Zhendong Yu [d], Jinling Xie [a,b], Ruihua Lin [f], Bo Peng [g], Liqiang Wang [b,g]

[a] Faculty of Geosciences and Engineering, Southwest Jiaotong University, Chengdu 611756, China
[b] MNR Key Laboratory of Metallogeny and Mineral Assessment, Institute of Mineral Resources, Chinese Academy of Geological Sciences, Beijing 100037, China
[c] Sobolev Institute of Geology and Mineralogy, Novosibirsk 630090, Russia
[d] The Third Geological Brigade of Jiangxi Geological Bureau, Jiujiang 332100, China
[e] Department of Geology and Geological Engineering, University Laval, Quebec GIV 0A6, Canada
[f] Tianjin Ji'ao Geological Exploration Technology Co., Ltd, Tianjin 300220, China
[g] College of Earth and Planetary Sciences, Chengdu University of Technology, Chengdu 611756, China

ARTICLE INFO

Handling editor: Li Tang

Keywords:
W-Mo-Cu mineralization
S-Pb-O isotopes
Oxygen fugacity
Vertical reverse zoning
Kunshan

ABSTRACT

The identification of reverse zoning in tungsten deposits is crucial, as it represents an atypical distribution of orebodies that may affect exploration and mining strategies. However, the exploration of such deposits remains challengeable due to uncertainties regarding the parageneses of polymetallic mineralization, the upper temperature limit of the formation of wolframite, and the evolutionary path of fluids, all of which influence the patterns of the distribution of ore mineralization. Recently, we have found that the Kunshan W-Mo-Cu deposit situated within the world-class Dahutang tungsten ore district in the middle segment of the Jiangnan Orogen, South China, is special for the vertical reverse zoning of W-Mo-Cu paragenetic mineralization. To trace the evolutionary paths of magmatic and deuteric hydrothermal fluids, estimate the redox conditions of magma crystallization, and determine the sources and temperatures of ore-forming fluids, we conducted a comprehensive study of the geochemical compositions of zircons and the S-Pb-O isotope systematics of quartz, wolframite and sulfide. We investigated the relationships between trace elements, oxygen fugacity (f_{O2}) and W-Mo-Cu parageneses, as well as the degree of contamination of parental magma by overlying metasediments. Our results indicate that the paragenetic W-Mo-Cu mineralization was triggered by a moderately reduced initial magma (ΔFMQ = −0.55 ~ -0.20) containing 41 % *meta*-igneous-dominated component ($\delta^{18}O_{magma}$ = +9.2 ‰) and metasediments ($\delta^{18}O_{WR}$ = +12.6 ‰). The vertical reverse zoning is characterized by proximal Cu mineralization located beneath the distal high-temperature (394 °C) tungsten mineralization zone and was formed by volatile-rich fluids within an open metallogenic system. We argue that the exploration of deposits with vertical reverse zoning should continue, despite the decrease in the grade of tungsten ore with depth, while the content of metal sulfides may likewise increase.

1. Introduction

The Jiangnan tungsten ore belt (JTOB) is located within the Jiangnan orogenic belt of South China and hosts numerous commercially important tungsten deposits, including the world-class Dahutang and Zhuxi ore districts (Fig. 1). Efficient evaluation and exploration of JTOB deposits necessitate in-depth analysis of initial magmas and their related ore-forming fluids, the formation of mineral parageneses, and the mechanisms and distribution patterns of mineralization. The tungsten deposits of the JTOB are of porphyry and skarn types and are typically associated with highly evolved calc-alkaline granitic magmatic rocks of Jurassic to Cretaceous ages emplaced in an intraplate tectonic setting (e.g., Mao et al., 2020; Wang et al., 2023). Recently, an increasing number of copper deposits associated with paragenetic tungsten, e.g., Dongleiwan, Tongjiangling and Wushan, have been identified and explored in the Middle-Lower Yangtze Depression (Wang et al., 2023). In those new

* Corresponding author.
E-mail address: pqm@swjtu.edu.cn (Q. Pei).

https://doi.org/10.1016/j.gr.2025.03.004
Received 14 July 2024; Received in revised form 28 March 2025; Accepted 29 March 2025
Available online 3 April 2025

Cu-W deposits, the W-Cu orebodies located beneath the previously mined copper orebodies appeared to possess a W-Cu to Cu metallogenic zoning upward or outward of pluton contact zones in the Wushan deposit (Wang et al., 2023).

The Kunshan W-Mo-Cu deposit, the objective of this paper, is located in the Dahutang tungsten ore field in the middle segment of the Jiangnan Orogen. The Dahutang ore field includes three types of orebodies: veinlet, breccia and quartz-vein (Xiang et al., 2015a). The primary W-Mo mineralization occurs along the outer or inner zones between numerous Mesozoic granitic stocks and country rocks (Neoproterozoic granodiorite batholiths or epi-metamorphic strata). The intrusion of Mesozoic granites along with dissolved fluid hydrothermally altered the surrounding rocks and formed diverse types of ore mineralization (Xiang et al., 2013c, 2015a; Zhang et al., 2013; Song et al., 2018). The Dahutang Mesozoic intrusions are highly differentiated S-type granites (Wei et al., 2018; Fan et al., 2019), whose origins have been studied before mostly for Hf-in-zircon isotopes (Xiang et al., 2015b; Zhang et al., 2018a). Nevertheless, the origin of the W-Mo-Cu mineralization associated with those granites remains debatable. One hypothesis argues that those intrusions originated from melting metasediments and Neoproterozoic granodiorites (Wei et al., 2018). Another hypothesis proposes that they originated from the mixing of melts from two magma chambers, each containing varying proportions of mafic lavas and pelites of the Shuangqiaoshan Group (SQSG) (Xiang et al., 2015b; Fan et al., 2019). Recently, the shift in the style of mineralization from initial quartz-wolframite (± molybdenum) stockworks to quartz-molybdenum-scheelite stockworks, and finally to quartz-chalcopyrite (± molybdate) veins was attributed to the progressive cooling of deuteric hydrothermal fluids in both the Kunshan and Dalingshang deposits (Peng et al., 2018; Zhang et al., 2018b). However, the W-Cu vertical reverse zoning of the Kunshan deposit, with proximal Cu mineralization that formed after distal W mineralization, is different from the zoning patterns observed in other deposits of the Dahutang ore field (Xiang et al., 2015a). However, no reasonable mechanisms for such vertical reverse zoning of the W-Mo-Cu mineralization in Kunshan, whether it was formed by multi-stage hydrothermal activity or at different stages of evolution of a single metallogenic system, remains uncertain. As a result, although they suggested a magmatic source of the W-Mo-Cu mineralization for the

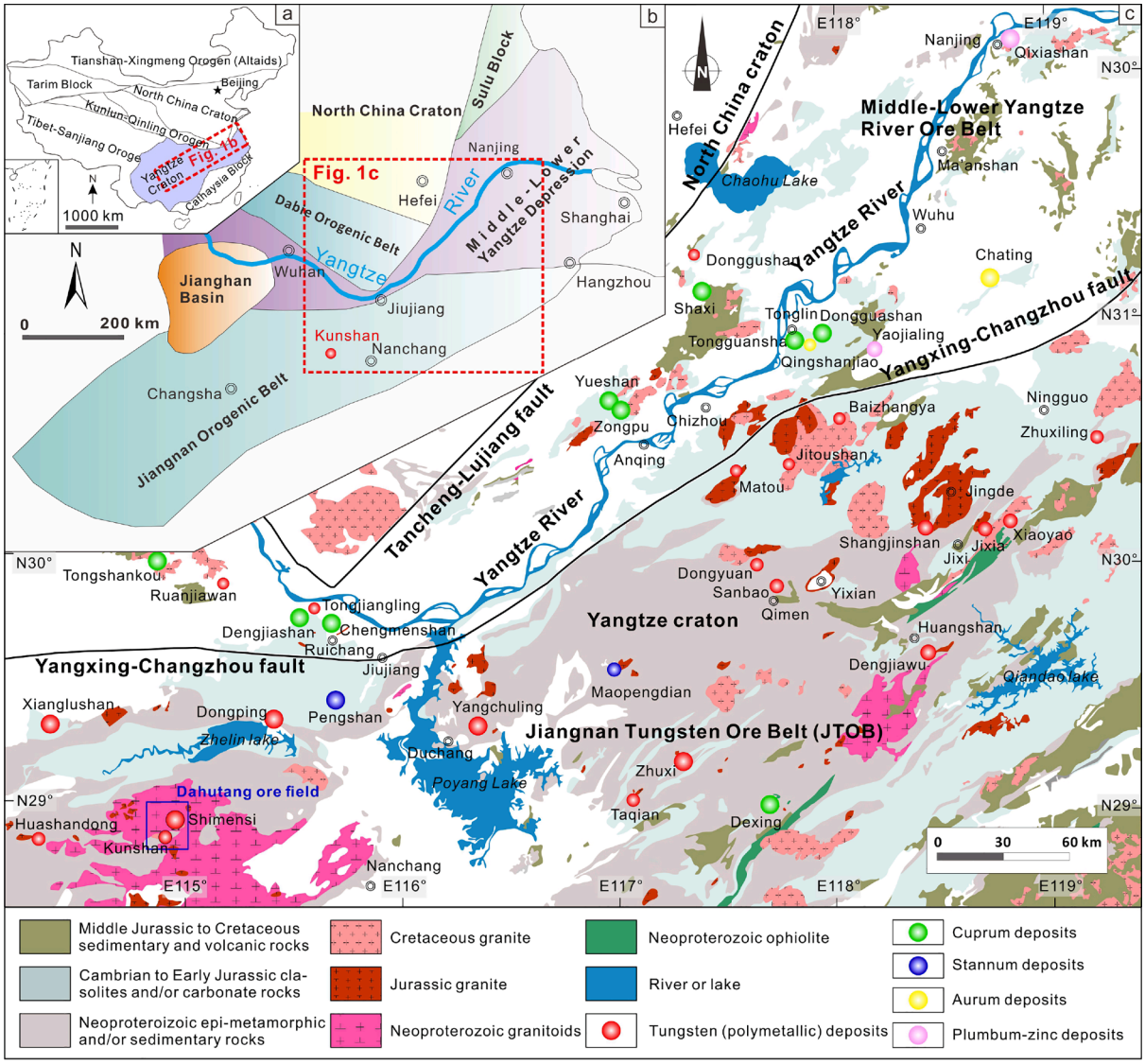

Fig. 1. (a) Tectonic map of China highlighting the major tectonic units and the Yangtze Block in South China. (b) Distribution of tectonic units in South China, showing the location of the Middle-Lower Yangtze River depression, the Jiangnan orogenic belt, and the geographical position of the Kunshan W-Mo-Cu polymetallic deposit. (c) Geological map of the Jiangnan tungsten ore belt (JTOB) and the Middle-Lower Yangtze River ore belt, illustrating the distribution of W, Cu, Sn, Au, and Pb-Zn deposits (modified after Wang et al., 2023; Mao et al., 2017).

whole Dahutang ore field (Zhang et al., 2018b; Fan et al., 2019), the nature of the granitic melts that controlled the geochemically distinct, but coeval W-Mo-Cu mineralization within a single deposit, such as the Kunshan deposit, remains poorly understood.

This study focuses on the Kunshan deposit of the Dahutang ore field, which is located in the mid-segment of the Jiangnan Orogen Belt and formed during the most intensive stage of the intraplate orogeny at ca.158 to 146 Ma. This study aims to understand the origin of granitic melts and potential relationships between the parageneses of polymetallic mineralization and their zoning, the redox state of parental magma, the modes of separation of ore-bearing fluids (void filling vs. permeable), and the type of metallogenic system (closed vs. open). We measured concentrations of trace elements and performed detailed studies of zircon U-Pb isotope systematics and quartz oxygen isotope systematics. In addition, we studied the oxygen and lead isotope systematics of wolframite and the sulfur isotope systematics of metal sulfides to determine the formation temperature of wolframite, identify the sources of W-Mo-Cu metals, and assess the influence of country rocks on mineral precipitation.

2. Geological settings

2.1. Regional setting

The Jiangnan orogenic belt is a tectonic zone situated between the Yangtze Craton and the Cathaysian Block. It consists of weakly metamorphosed Neoproterozoic sedimentary-volcanic rocks, Neoproterozoic granitoids and subordinate mafic rocks. It extends more than 1,500 km from northern Guangxi to central Jiangsu (Zhou et al., 2002) (Fig. 1b). The Jiangnan orogenic belt was formed by Paleoproterozoic to Neoproterozoic geological events, including the formation of the Yangtze basement and the convergence and separation of the Yangtze and Cathaysia blocks (Yao et al., 2014). During the Paleozoic (~420 Ma), the Jiangnan orogenic belt was uplifted and partially dismembered (Xue, 2021). During the Mesozoic period, intraplate activity in the Jiangnan orogenic belt initiated diagenetic and metallogenic processes that varied in timing and intensity (Yao et al., 2014; Xiang et al., 2015b).

The JTOB is located within the NEE-SWW striking Jiangnan orogenic belt and extends east of it (Fig. 1c). The estimated WO_3 reserves of the JTOB are 6.06 million tons (Mao et al., 2020). The Mesozoic reactivation of older fault systems created favorable conditions for the upwelling of highly evolved silica-rich magmas and fluid migration and was related to the formation of tungsten polymetallic deposits (Xiang et al., 2013c; Song et al., 2018; Song et al., 2022). Two distinct types of Mesozoic granites are associated with mineralization in the JTOB: metaluminous granodiorite (e.g., Dongyuan, Zhuxiling, Dengjiawu, Sanbao, Shangjinshan, Matou, and Gaojiabang, Fig. 1c) and peraluminous biotite or muscovite granites (e.g., Dahutang, Zhuxi, and Xianglushan, Fig. 1c). The peraluminous granites represent primary sources of world-class tungsten deposits (Mao et al., 2020; Wang et al., 2023). In the Jiangnan orogenic belt and at its eastern extension of special importance are the Proterozoic SQSG metasedimentary rocks, which consist primarily of slate and sandstone. The intercalated spilite-quartz keratophyre association layers probably served as initial sources of the Mesozoic tungsten, gold, silver and copper mineralization (Xiang et al., 2015b).

2.2. Local setting

The Dahutang ore field comprises various tungsten polymetallic deposits, including the super-large Shimensi and Shiweidong deposits, the large-scale Yikuangdai and Pingmiao deposits, as well as several medium- to small-scale deposits such as Kunshan, Dalingshang and Maogongdong. Most orebodies extend from SE to NE and are aligned at intervals of 2.5 to 3.5 km (Fig. 10). The Kunshan deposit hosts medium reserves of tungsten and molybdenum and a small reserve of copper (Ye et al., 2016). Previous studies have identified that the W-Mo-Cu polymetallic mineralization in the Kunshan deposit of quartz-veinlet-cluster type (Zhang et al., 2018a; Lin et al., 2023). The Neoproterozoic granodiorites intrude the Anlelin Formation of the SQSG, which serves as a host rock of the orebodies of the Shimensi deposit, leaving only sporadic outcrops in the NW and SE parts of the Kunshan deposit. The Kunshan Late Jurassic intrusions are high-K calc-alkaline granites: gray porphyritic biotite granite (G1, Fig. 2a), gray fine-grained biotite granite (G2, Fig. 2d), grayish-white fine-grained granite (G3, Fig. 2g), and granite porphyry (G4, Fig. 2j). The W-Cu-Mo mineralization is associated with the G1-G3 granites, whereas the G4 granite is a barren post-mineralization intrusion.

There are three types of mineralization in the Kunshan deposit: (i) quartz-veinlet-cluster (primary type); (ii) quartz-vein; and (iii) veinlet-disseminated (Ye et al., 2016). These diverse types reflect a complex geological history and multi-stage hydrothermal processes, which were responsible for the formation of the deposit. The quartz-veinlet-cluster-type orebodies are structurally controlled by two major structural trends: (i) early NEE-SWW trending fractures and faults, which host the most productive quartz veinlet clusters and are parallel to the subvertical stratification and foliation of the Proterozoic *meta*-sandstone, phyllite, and slate (Fig. 2c); (ii) later NE-SW trending faults, which control the distribution of the Late Jurassic granites. The most productive type of orebody is the quartz-veinlet-cluster, which is distributed along the NEE-SWW to EW-trending swarm of quartz veinlets (60°-85°) that host W-Mo-Cu mineralization (Fig. 2c, Fig. 3). The quartz veinlet clusters occur within the Proterozoic *meta*-sedimentary rock and are situated within a 600 m vertical range at the outer contact zone between the SQSG strata and the Late Jurassic intrusions (Fig. 3). The processes of hydrothermal alteration include hornfelsization, silicification, greisenization, sericitization, muscovitization, chloritization and kaolinization. Copper mineralization is closely associated with chloritization, whereas tungsten and molybdenum mineralization are predominantly linked to greisenization (Ye et al., 2016). The molybdenum-bearing quartz veins intersect the earlier wolframite-quartz veins and are, in turn, crosscut by the later the chalcopyrite-quartz veins. The progression of mineral assemblages, from early wolframite to molybdenum and subsequently chalcopyrite (Zhang et al., 2018b; Lin et al., 2023), along with their complex interrelationships, indicates a multifaceted history of hydrothermal events that triggered mineralization.

Wolframite orebodies occur at elevations above 920 m, where tungsten mineralization predominates and molybdenum mineralization is relatively subordinate (Fig. 3). In contrast, molybdenum mineralization dominates at elevations below 920 m (Fig. 3). For detailed information on the mineral parageneses of the Kunshan deposit, refer to Table S1. Thus, three stages of mineralization have been identified: wolframite-dominated Stage I, transitional from wolframite to molybdenite and scheelite Stage II, and chalcopyrite-dominated Stage III (Table S1). These stages fit the pattern of metal-mineral crystallization from oxide to sulfide minerals, as was previously observed in the Dahutang ore field (Xiang, 2012; Xiang et al., 2015a; Xiang et al., 2017). Similar successions of changes in mineral assemblages and typomorphic minerals can be observed within individual quartz veins formed during each separate mineralization episode (see below). Early to late mineralization was synchronous with the transition from vein tops to vein bottoms, or from vein margins to vein cores (Fig. 2i, l). The Kunshan deposit exhibits an atypical distribution of orebodies, with high-temperature wolframite, minor molybdenum and cassiterite in the distal A- and B-zones (Stage I) (Fig. 3, Table S1). The wolframites in the A-zone are located at the highest elevation and heavily eroded, they probably crystallized rapidly, forming fine-grained and thin-plate-like structures. Wolframites particles in the B-zone are denser and larger, reflecting a more stable ore-forming environment. Molybdenum and scheelite are primarily concentrated in the C-zone (Stage II), while a low-temperature chalcopyrite (± molybdate) assemblage is dominant in the D-zone (Stage III). In the D-zone, chalcopyrite occurs along the cleavage fissures of molybdenite or partially encloses molybdenite. The

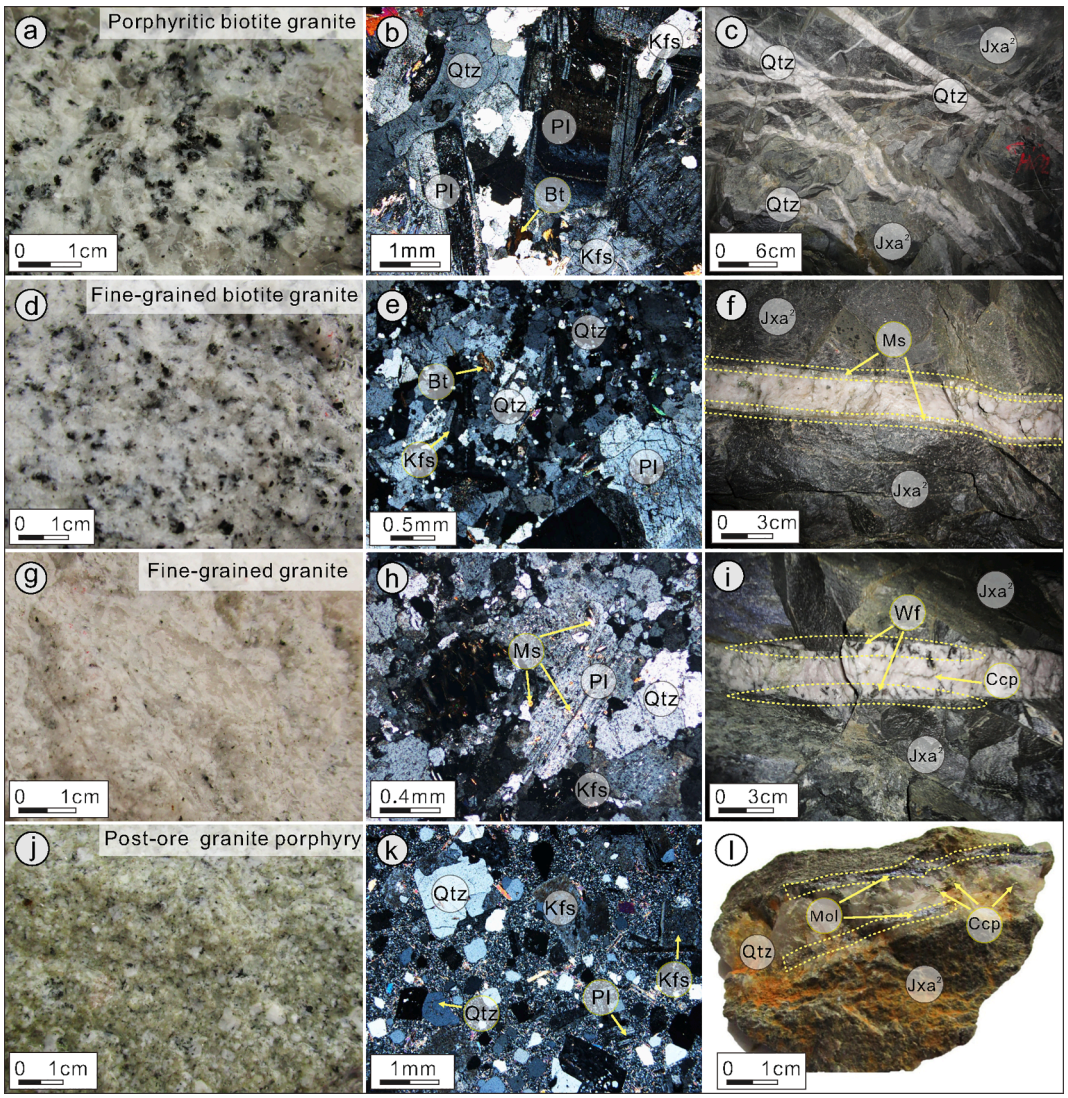

Fig. 2. Representative specimens and photomicrographs of granites and ore-bearing quartz veins of the Kunshan W-Mo-W polymetallic deposit: (a) gray porphyritic biotite granite (G1); (b) a photomicrograph of porphyritic biotite granite; (c) crisscrossed orebodies of quartz-veinlet-cluster-type; (d) gray fine-grained biotite granite (G2); (e) a photomicrograph of fine-grained biotite granite; (f) muscovite hosted by selvages on both sides of ore-bearing quartz vein; (g) grayish-white fine-grained granite (G3); (h) a photomicrograph of fine-grained granite; (i) early-stage wolframite in selvages on both sides of the quartz vein and late-stage chalcopyrite hosted a vein core; (j) post-ore granite porphyry (G4); (k) a photomicrograph of granite porphyry; (l) early-stage molybdenite in selvages on both sides of a quartz vein and late-stage chalcopyrite hosted by the quartz vein core. Mineral abbreviations: Qtz = quartz, Pl = plagioclase, Kfs = K-feldspar, Bt = biotite, Ms = muscovite, Mol = molybdenite, Wf = wolframite, Ccp = chalcopyrite, Jxa^2 = *meta*-residual sandstone, phyllite, and slate.

E-zone (Stage IV), characterized by the pinch-out of quartz veins, lacks significant ore mineralization. This sequence is characterized by vertical reverse zoning, progressing from distal to proximal zones (A-zone to E-zone) and from higher to lower temperatures (Fig. 3). These findings suggest similar evolutionary paths of mineralization and imply gradual changes in the temperature of ore formation and the composition of ore mineralization.

3. Methods

3.1. Sampling

Forty fresh samples were collected from the Kunshan deposit, including nine quartz mineral samples separated from granites. Granites G1, G2, and G3 (KS1-1 to KS1-4; KS2-1 to KS2-4, and KS3-1 to KS3-4) were taken from the ZK0-1 drill core. Three granite porphyries (KS4-1, KS4-2, and KS4-3) were taken from a mine adit at an elevation of + 1020 m. Eight wolframite samples (KS5-1 to KS5-8) were collected from surface outcrops and adits at various elevations. Additionally, eight molybdenum samples (KS6-2, KS6-3 to KS6-6, KS6-11, KS6-12 and KS6-16) were obtained from drill cores and adits. Among the samples of granites, two Late Jurassic ore-related granites, G2 and G3, have not been previously reported. Zircons from the four granite samples were separated at the Geological Service Co., Ltd., Langfang, Hebei Province.

3.2. Oxygen, sulfur, and lead isotope analysis

As intracrustal igneous rocks and supracrustal sedimentary rocks exhibit different $\delta^{18}O$ characteristics, they can provide valuable insights for understanding the properties of the original magma (e.g., Giletti, 1986; Cherniak and Watson, 2003; Trail et al., 2009; Keyser et al., 2023). The ratios of oxygen isotopes in whole-rock samples are highly sensitive for post-crystallization alteration which makes $\delta^{18}O$ studies of granites more reliable if conducted on monomineral separates rather than on whole-rock powders. Minerals with higher closure temperatures (e.g., zircon, garnet, and quartz) are more resistant to post-

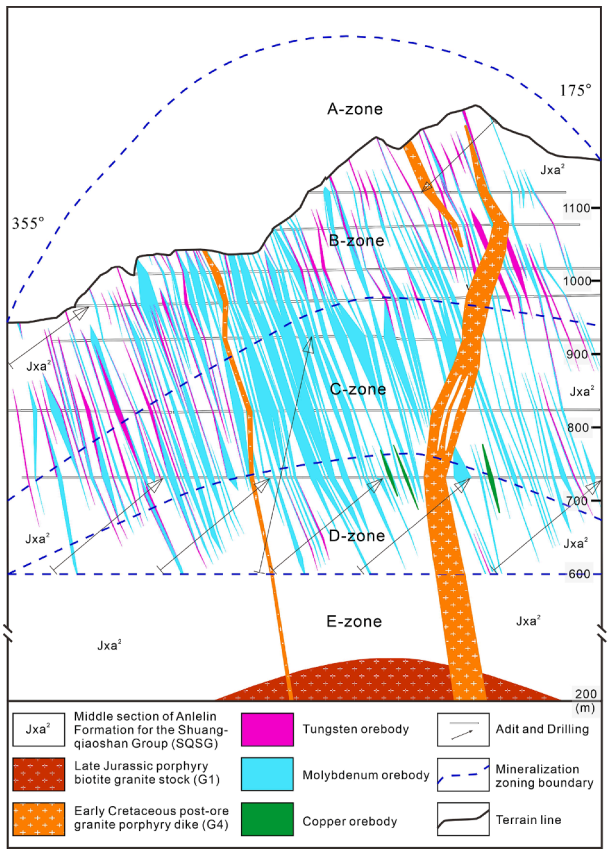

Fig. 3. A NS cross-section of the Kunshan W-Mo-Cu polymetallic deposit.

crystallization or sub-solidus oxygen isotope exchanges with external fluids. Thus, these minerals provide more robust evaluations of main characteristics of magma during its ascent (e.g., Trail et al., 2009; Caracciolo et al., 2022; Keyser et al., 2023). In our study, the O-S-Pb isotope analyses were performed at the Beijing Research Institute of Uranium Geology, Beijing. Wolframite and quartz grains were manually selected under a microscope from disaggregated samples. The quartz and wolframite samples were ground to powder (finer than 200 μm) and dissolved in pure BrF_5 in Ni tubes under high-temperature and vacuum conditions to release oxygen. Impurities (SiF and BrF) were removed via freezing, and the pure oxygen was captured directly by freezing it onto a 5Å molecular sieve using liquid nitrogen. Subsequently, the pure oxygen reacted with a hot carbon rod to generate CO_2 gas. Carbon dioxide gas, obtained through cryogenic methods, was introduced into a gas isotope mass spectrometer to measure the oxygen isotopic compositions. The $\delta^{18}O_{V\text{-}SMOW}$ values were calculated by comparing the oxygen isotopic compositions of the samples with those of the standards, using formula $\delta^{18}O = [(^{18}O/^{16}O)_{sample}/(^{18}O/^{16}O)_{standard})\text{-}1] *1000$. All the $\delta^{34}S_{V\text{-}CDT}$ values were determined with an accuracy better than 0.2 ‰. For Pb isotopes, the precision of the $^{204}Pb/^{206}Pb$ ratios was better than 0.05 %, whereas the precision of the $^{208}Pb/^{206}Pb$ ratios did not exceed 0.005 %.

3.3. Zircon isotopes and trace elements

Zircons were mounted in epoxy resin and polished to a thickness of 20 μm. The sites for ablation were selected manually based on CL images and cleaned with 3 % HNO_3 prior to analysis. The isotope and elementary analyses were conducted simultaneously using an Agilent 7500a instrument at the Hefei University of Technology. We used a Coherent GeoLasPro laser ablation system (USA) equipped with a ComPex102 ARF Excimer laser operating at a wavelength of 193 nm, a 32-μm-diameter beam spot and an energy density of approximately 15 J/cm^2. The external and internal standards are NIST610 glass and ^{91}Zr, respectively. ICPMSDATACAL software (Liu et al., 2008) was used for blank signal selection, element quantification, and isotopic calculations. Radiometric dating plots were generated using "IsoplotR" (Vermeesch, 2018).

3.4. Zircon composition index estimates

Zircon is an early crystallizing accessory mineral present in most igneous rocks. It is highly resistant to alteration, surface weathering, and other external processes (Pirkle and Podmeyer, 1993; Lin et al., 2024). To assess whether the analyzed grains were inherited or crystallized in-situ, for trace element analysis, we analyzed zircon grains with known U-Pb ages. The trace element composition of zircon reflects the initial conditions of crystallization during magma cooling. Consequently, the ratios of Ce^{4+}/Ce^{3+}_{zircon} and Ce^{4+}/Ce^{3+}_{melt} as estimated from zircon trace element data, serve as indicators of the magma redox state (Ballard et al., 2002; Trail et al., 2012; Loader et al., 2022). To calculate the Ce^{3+} distribution coefficient between zircon and melt, we perform linear regressions of entire rare earth element (REE) spectra versus ionic radii. The distribution coefficient of Ce^{4+} was determined by calculating the regressions of the zirconium, hafnium, uranium, and thorium versus the ionic radii (Burnham and Berry, 2012).

To estimate the oxygen fugacity (f_{O2}) of the Kunshan granitic magmas, we used two methods. The first method utilizes a calibration model that links f_{O2} and four key parameters: melt composition, water content, Ce^{4+}/Ce^{3+}_{Melt} ratios and temperature (Smythe and Brenan, 2015, 2016). The whole-rock composition, which we consider as a composition of an initial melt, and the content of water both affect the ratios of non-bridging oxygen to tetrahedral cations (NBO/T). For this study, we assumed that the melts of the G1-G4 granites contained 5 wt% water and calculated the Ce^{4+}/Ce^{3+}_{Melt} ratios based on the lattice strain model. The geothermometry of zircon formation was calculated using the activities of SiO_2 and TiO_2 (α_{TiO2} and α_{SiO2}) and the content of titanium in zircon (Ferry and Watson, 2007). The obtained f_{O2} values, if presented as logarithmic units (log f_{O2}), exhibit an error range of 1.3–2.6. For detrital zircons or xenocrystic zircons, it is not possible to estimate f_{O2}, as it requires the content of water in the melt and the geochemical compositions. In contrast, the Loucks et al. (2020) model considers only the amounts of titanium, cerium, and initial uranium in age-corrected zircons. For discussion, we used trace element data from those zircon grains, which fit the following criteria: (i) LREE Index (LREE-I) > 10 (Bell et al., 2016), (ii) Ti < 50 ppm, and (iii) La < 1 ppm. This helps minimize the impact of hydrothermal alteration, inclusions, and inherited cores. For the experiments, we used a 32 μm diameter laser beam.

4. Results

4.1. Whole-rock element compositions of the G1-G4 granites

All Kunshan G1-G4 samples are petrographically (Fig. S1) and geochemically (Table S2) granites. They are characterized by high SiO_2 (71.44–78.27 wt%), Al_2O_3 (11.45–14.47 wt%), and K_2O (3.99–6.70 wt %) and low TiO_2 (0.08–0.34 wt%), CaO (0.47–1.88 wt%) MgO (0.18–0.71 wt%), $Fe_2O_3^T$ (0.89–3.92 wt%), and MnO (0.01–0.05 wt%) at a relatively medium content of Na_2O (2.20–3.32 wt%). The A/CNK ratios range from 1.03 to 1.30, whereas the K_2O contents vary between 3.99 % and 6.70 %. Therefore, the granites under study belong to the peraluminous high-K calc-alkaline series. The values of loss on ignition are below 2 %, indicating a low degree of secondary alteration.

In terms of the whole-rock trace element characteristics, the total rare earth element ($\sum$REE) content of the samples ranges from 22 to 150 ppm. They are enriched in light REEs ($(La/Sm)_N$ = 2.33–4.61) and depleted in heavy REEs ($(Gd/Yb)_N$ = 0.02–0.35), with negative peaks at Eu (Eu/Eu* = 0.25–0.52; Table S2). The G1-G4 granites possess a 'V-

shaped' REE distribution pattern with a right-dipping trend (Fig. 4a). The enrichment in Rb and U (Fig. 4b) suggests potential dehydration melting of mica within the magmatic source region. The Eu troughs and depletions in Ba, Sr and Ti suggest the separation of plagioclase during magmatic differentiation or the presence of plagioclase residues in the magma source region (Li et al., 2007).

The whole-rock compositions of the G1-G3 ore-related granites are generally similar but display systematic decreases in ∑REE, $(La/Yb)_N$ and Eu anomalies from G1 to G3 and increase in SiO_2, the differentiation index (DI), and $TE_{1,3}$(tetrad effect, Irber, 1999) (Table S2), suggesting gradual evolution of the parental melts.

In summary, the Kunshan granites are highly differentiated, with high SiO_2 contents and low MgO, CaO, TiO_2, Sr and Ba contents. In addition, the Kunshan granites are compositionally similar to the Mesozoic granites of the Dahutang ore field, suggesting a common source or compositionally similar parental magma source (Xiang et al., 2015b).

4.2. U-pb zircon ages

The zircons separated from the G1-G4 granites (KS1-1, KS3-1, KS2-1, and KS4-3) are 80 to 200 μm long subhedral to euhedral granular crystals, light to dark grey, and possess oscillatory zoning CL images (Fig. 5), indicating their magmatic origins (Hoskin, 2000). The Th/U ratios range from 0.05 to 1.57, 0.05 to 1.79, 0.06 to 2.73, and 0.01 to 0.91, respective to the four groups, G1 to G4 (Table S3). The G1 to G4 zircons yield $^{206}Pb/^{238}U$ ages ranging from 146 to167 Ma: 157.6 ± 1.6 Ma, 157.2 ± 1.5 Ma, 154.9 ± 1.6 Ma and 145.6 ± 2.2 Ma, respectively (Fig. 5). These results indicate that the ore-related granites (G1-G3) were emplaced at ca. 157–155 Ma, while the post-ore granite (G4) was emplaced at ca. 146 Ma.

4.3. S-Pb-O isotopic compositions

Quartz from the Kunshan ore-related granites G1-G3 yields $\delta^{18}O$ values ranging from + 11.2 ‰ to + 13.9 ‰, with an average of 12.1 ‰ ($1\sigma = 0.79$ ‰, $n = 11$; Table S4). The $\delta^{18}O$ value of 16.9 ‰ for quartz in sample KS1-3 was excluded due to its deviation from the normal range. The range of $\delta^{18}O$ values in quartz from the G1-G3 granites is + 11.2 ‰ to + 13.9 ‰ (avg. 12.3 ‰) for G1, +11.4 ‰ to + 12.9 ‰ (avg. 12.1 ‰) for G2, and + 11.3 ‰ to + 12.8 ‰ (avg. + 11.9 ‰) for G3 (Table S4). Among these granites, the G1 granite has the highest average quartz $\delta^{18}O$ value of 12.3 ‰. The relatively consistent $\delta^{18}O$ values suggest a shared origin of the Kunshan G1-G3 granites. The values of $\delta^{18}O$ in quartz from the G1 granite are more variable than those from the G2 and G3 granites ($\delta^{18}O_{Qtz} = +11.98 \pm 0.59$ ‰, $n = 8$; Table S4), possibly due to the influence of thick strata of the SQSG (Gong et al., 2023).

Sulfur isotope measurements were performed on eight molybdenite samples (Table S5). The $\delta^{34}S$ values are in a relatively narrow range of −0.7 ‰ to 1.5 ‰ ($n = 8$) suggesting sulfur isotopic homogeneity (Fig. S2 and Table S5). This consistency implies that all molybdenite samples likely originated from a single source.

The Pb isotope systematics were studied in eight samples of Pb-bearing wolframites. Most of the lead isotopic compositions plot closely to cluster around the radiogenic values, indicating their primary source region (Table S6).

4.4. Trace element compositions of zircon

The contents of Y, ΣREE and P in the G4 zircons are much more variable compared to those in the G1-G3 granites (Table 1). In addition to oscillatory zoning, the zircons are magmatic due to their low ΣREE values and the absence of notable enrichment in middle REE (MREE), which clearly distinguishes them from hydrothermal zircons (Fig. 6a) (Hoskin, 2005). All zircon grains from the G1–G4 granites of the Kunshan deposit exhibit significant enrichments in heavy REE (HREE) and Ce, along with pronounced negative Eu anomalies (Eu/Eu*) (Fig. 6a, b). Zircons from G4 display slightly higher REE concentrations than those from G1-G3. The variation in Eu/Eu* ratios is attributed to the differing geochemical behaviors of Eu^{2+} and Eu^{3+}, which reflects oxidation conditions during zircon crystallization (Whitehouse and Kamber, 2002; Burnham and Berry, 2012). The ranges of the Eu/Eu* ratios are as follows: 0.13–0.33 (avg. 0.20) for G1; 0.10–0.49 (avg. 0.20) for G2; 0.10–0.34 (avg. 0.19) for G3; and 0.02–0.36 (avg. 0.10) for G4. These consistently low Eu/Eu* values, coupled with pronounced negative Eu anomalies, are characteristic of the G1-G4 granites (Fig. 6a).

4.5. Zircon Ce4+/Ce3 + ratios, crystallization temperatures and redox states

To avoid contaminated and/or inherited zircons, we calculated the Ce^{4+}/Ce^{3+}_{Zircon} in the zircons, their crystallization temperatures ($T_{Ti\text{-}in\text{-}zircon}$), and the f_{O2} only for the Late Jurassic to Early Cretaceous magmatic zircons with concordance better than 90 % (Table S7). Based on the presence of quartz and sphene (Ye et al., 2016), α_{TiO2} and α_{SiO2} are assumed to be 1 and 0.7, respectively (Ferry and Watson, 2007; Claiborne et al., 2010). Zircons with exceptionally high or low Ti concentrations were excluded to avoid overestimating or underestimating crystallization temperatures. The $T_{Ti\text{-}in\text{-}zircon}$ values calculated for the G1-G4 granites using the Ti-in-zircon thermometer were as follows: 621–824 °C (avg. 698 ± 52 °C, $n = 28$) for G1, 614–829 °C (avg. 725 ± 62 °C, $n = 24$) for G2, 640–827 °C (avg. 724 ± 47 °C, $n = 28$) for G3, and 654–867 °C (avg. 746 ± 56 °C, $n = 13$) for G4 (Fig. 7a).

The Ce^{4+}/Ce^{3+}_{Zircon} ratios were estimated using the trace element compositions of granites and the concentrations of hafnium, zirconium, uranium, thorium, and REEs in zircons (Burnham and Berry, 2012; Trail

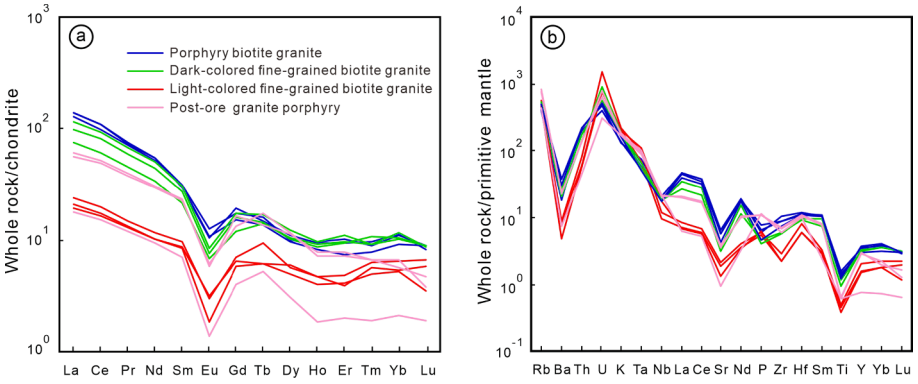

Fig. 4. Chondrite-normalized REE patterns (a) and primitive mantle-normalized spider diagrams (b) of granites from the Kunshan tungsten polymetallic deposit (normalized values from Sun and Mcdonough, 1989).

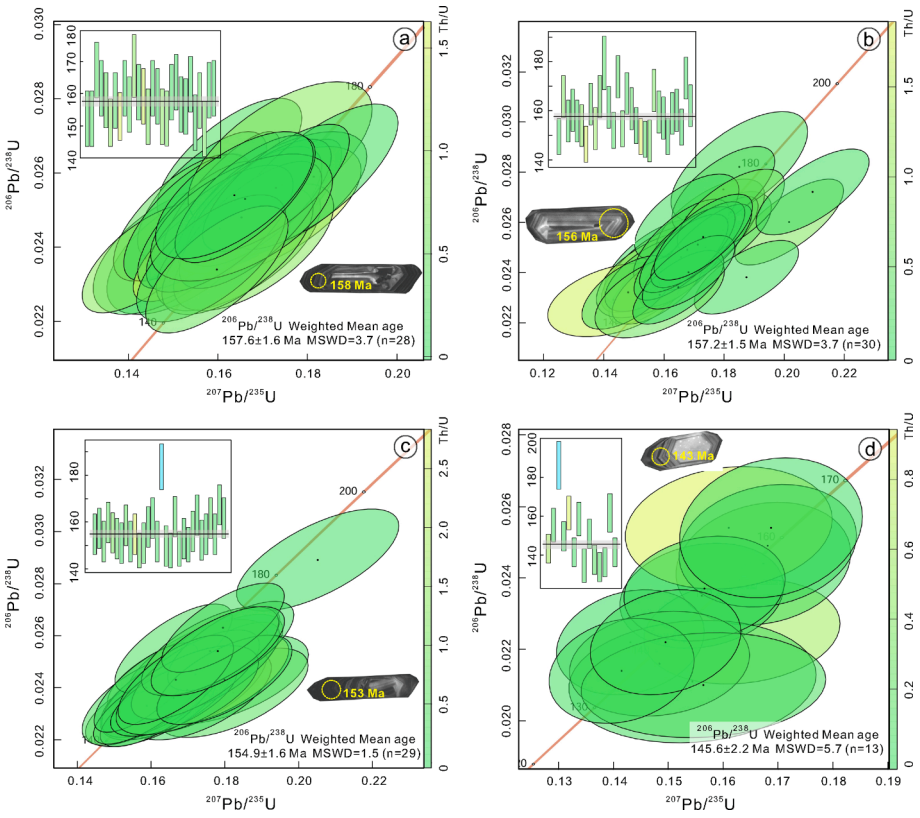

Fig. 5. Zircon U-Pb concordia diagrams for (a) sample KS1-1, (b) sample KS3-1, (c) sample KS2-1, and (d) sample KS4-3 from the Kunshan tungsten polymetallic deposit.

et al., 2012). The Ce^{4+}/Ce^{3+}_{Zircon} ratios of the G1, G2 and G3 granites are typically greater than 60, with mean values of 92, 87 and 68, respectively (Fig. 7a, Table 1). The G4 zircons exhibit notably lower Ce^{4+}/Ce^{3+}_{Zircon} ratios, averaged at 58 (Fig. 7a, Table 1). The Ce^{4+}/Ce^{3+}_{Zircon} ratios progressively decrease from the G1 granite stock, through the G2 and G3 granite dikes, to the post-ore G4 granite dikes (Fig. 7a).

A variety of methods have been proposed to estimate zircon f_{O2} values, which reflect the f_{O2} of the initial magma (Trail et al., 2012; Smythe and Brenan, 2015; Zou et al., 2019; Loucks et al., 2020). Among the Kunshan G1-G4 granite samples, zircons from the G1, G2 and G4 granites yield relatively low f_{O2} values. Based on the Smythe and Brenan (2016) oxybarometer, the average ΔFMQ^a values are −1.12 ($n = 30$) for the G1 granite, −0.25 ($n = 30$) for the G2 granite, and −0.72 ($n = 29$) for the G4 granite (Table S7). The G3 granite samples exhibit relatively high f_{O2} values, with an average ΔFMQ^a of + 1.53 ($n = 30$) (Fig. 7b, Table 1). According to the model of Loucks et al. (2020), the average ΔFMQ^b values for the G1-G4 granites are −0.20 ± 1.30 ($n = 19$) for G1, −0.55 ± 1.29 ($n = 19$) for G2, −0.28 ± 1.09 ($n = 21$) for G3, and −0.82 ± 0.73 ($n = 4$) for G4 (Fig. 7b, Table 1). In general, the ΔFMQ^b data exhibit a gradual decrease from G1 to G4. The calculated values of f_{O2} are not highly variable (Fig. 7b), indicating that this method (Loucks et al., 2020) provides estimates closer to real values of f_{O2}. The discrepancy between the two models arises from inaccuracies in the assumed water content of the intrusions in the model proposed by Smythe and Brenan (2016).

5. Discussion

5.1. Sources of mineralization

5.1.1. Magmatic sources

The Mesozoic magmatic activity significantly affected the formation of W, Cu and Mo deposits at Dahutang. Mineralization was triggered by the emplacement of Late Jurassic to Early Cretaceous granitoids. The Kunshan deposit formed during an early stage of tungsten-polymetallic mineralization in the Dahutang ore field, as the Kunshan granites yielded the earliest emplacement ages of ca. 157 to 145 Ma (Fig. 5, Table S3). The 151.0 to 148.7 Ma Re-Os isotope isochron age of molybdenite (Xiang et al., 2013b; Zhang et al., 2013; Zhang et al., 2016; Lin et al., 2023) and the 143.7 to 139.2 Ma mineralization (Mao et al., 2013) suggest that the magmatic activity in the Kunshan area began at 157.6 Ma, i.e., nearly 10 Ma earlier than that in the Shimensi deposit (148 Ma, Fan et al., 2019). This zonal pattern could result from the different properties of the SQSG country rocks, which are more fractured than the Neoproterozoic granodiorite batholith. According to the equation $Zr^{2+}+SiO_4^{2-} = (REE)^{3+} + PO_4^{3-}$, REE^{3+} substitutes Zr^{2+} in zircon via monazite (Burnham and Berry, 2017). The Kunshan granites are 'hybrid' S-type granites, i.e., formed from a mixture of sedimentary and igneous protoliths. Evidence for this is provided by the $(REE + Y)_{mol}/P_{mol}$ ratios of zircons from the G1-G4 granites, which are less than 1.15 (0.80, 1.06, 0.86, and 0.75, respectively; Fig. 8a), along with P concentrations higher than 750 ppm and moderate ratios of Ce/U and Th/U (Fig. 8b; Roberts et al., 2024).

The $\delta^{18}O$ values of quartz and feldspar in the fine-grained granite from the Dahutang ore field imply oxygen isotope equilibrium during closed-system fractional crystallization (for details, refer to Text S1). However, the estimated $\delta^{18}O_{Qtz}$ value is approximately + 10.05 ‰, which is 2 ‰ lower than the $\delta^{18}O_{Qtz}$ value of + 11.98 ‰ observed in the fine-grained G2 and G3 granites, as estimated using the fractionation equation of quartz and zircon (Text S1). The observed 2 ‰ increase in the $\delta^{18}O_{Qtz}$ value suggests the assimilation of high-$\delta^{18}O$ crustal components, rather than the rapid mixing of multi-batch magma. This interpretation is supported by the absence of high-$\delta^{18}O$ metasediment-derived zircons (ranging from + 8 ‰ to + 11 ‰; Fig. 9c, Kemp et al., 2007) and the compatibility of quartz with a $\delta^{18}O_{Qtz}$ value of + 10.05 ‰, consistent with low-$\delta^{18}O$ zircon values (avg. + 7.47 ‰, higher than

Table 1
Summary of In-situ element compositions (in ppm) of zircons from the Kunshan tungsten-molybdenum-copper deposit.

Sample	porphyritic biotite granite (G1)			gray fine-grained biotite granite (G2)			grayish-white fine-grained granite (G3)			Granite porphyry (G4)		
	Min	Max	Mean	Min	Max	Mean	Min	Max	Mean	Min	Max	Mean
La	–	21.55	2.08	–	44.62	3.40	–	16.60	1.43	–	18.83	2.13
Ce	0.83	142.88	33.74	8.40	215.43	49.00	9.34	141.66	38.32	0.89	121.10	17.11
Pr	0.02	11.38	1.11	0.01	22.33	2.07	0.07	8.03	0.98	0.05	6.99	0.97
Nd	0.56	61.93	8.01	0.48	123.94	14.11	1.09	42.73	8.29	0.70	33.31	6.27
Sm	1.69	34.40	9.25	1.94	61.14	14.68	3.51	37.99	12.62	2.87	32.09	10.43
Eu	0.10	5.68	1.40	0.24	7.64	2.07	0.45	7.94	1.82	0.08	2.86	0.81
Gd	13	142	49	14	165	66	14	147	65	18	200	66
Tb	6	40	18	6	49	23	5	51	24	7	87	28
Dy	82	478	230	88	596	281	67	589	284	102	976	349
Ho	34	183	88	35	220	104	27	212	104	36	309	122
Er	171	866	408	172	1026	473	126	892	469	119	1212	521
Tm	39	198	91	41	251	106	29	194	104	21	246	110
Yb	378	1921	875	410	2545	1028	300	1844	992	172	2165	1018
Lu	70	341	161	79	466	186	58	321	180	29	355	178
Y	1039	5334	2563	1053	6503	3030	780	5993	3028	1107	9342	3671
Ti	2	15	5	2	4915	177	2	61	8	2	22	9
Hf	9083	18,571	13,864	8766	17,648	13,627	10,272	19,989	14,094	10,546	29,368	13,854
Th	60	3742	785	165	4603	1041	194	9604	1288	69	1399	308
U	407	11,872	3081	402	17,472	3993	798	11,436	3663	317	16,839	3210
P	346	2615	994	383	19,646	1561	627	3778	1266	777	5768	2299
Nb	0.90	31.44	9.66	2.38	77.09	15.03	2.84	69.12	16.08	0.66	12.55	4.81
Ta	0.56	15.58	5.45	0.77	24.14	7.31	1.64	26.47	9.53	0.26	30.65	4.17
Ce/U	0.00	0.09	0.01	0.00	0.08	0.02	0.00	0.06	0.01	0.00	0.12	0.01
Th/U	0.05	1.57	0.36	0.05	1.79	0.40	0.06	2.73	0.43	0.01	0.91	0.22
Yb_N/Gd_N	8	39	25	9	51	22	8	39	22	3	50	22
LREE	5	269	56	11	420	85	16	186	63	6	197	38
HREE	820	4121	1920	847	5282	2268	626	4124	2223	618	5371	2392
∑REE	833	4390	1976	858	5703	2353	659	4263	2286	635	5425	2430
Eu/Eu*	0.03	0.33	0.19	0.10	0.49	0.20	0.10	0.34	0.18	0.02	0.36	0.12
[A]Ce/Ce*	2	152	48	2	284	46	2	156	46	3	97	19
[B]$T_{Ti\text{-}in\text{-}zircon}$(℃)	621	824	699	544	2301	795	640	1000	732	654	867	757
[C]Ce^{4+}/Ce^{3+}_{zircon}	14	272	92	10	437	87	4	209	68	0	344	58
[D]log f^a_{O2}	−22.42	−12.99	−18.34	−20.63	0.32	−15.99	−18.14	−9.24	−14.89	−24.09	−11.33	−16.52
[E]ΔFMQ[a]	−5.19	1.67	−1.12	−2.48	2.48	−0.25	−0.29	3.79	1.53	−5.69	3.82	−0.72
[F]log f^b_{O2}	−21.33	−12.65	−17.90	−20.27	−12.46	−17.21	−19.82	−13.10	−16.98	−18.49	−14.35	−16.93
[G]ΔFMQ[b]	−2.42	2.01	−0.20	−3.37	2.12	−0.55	−2.08	1.57	−0.28	−1.75	−0.03	−0.82
[H]LREE-I	23	318	114	14	477	102	22	244	96	12	616	155

The symbol "-" indicates values below the detection limit.
[A] Ce/Ce* ratios are method from Loader et al. (2017).
[B] $T_{Ti\text{-}in\text{-}zircon}$ (℃) Crystallization temperature based on the revised Ti-in zircon thermometer following Ferry and Watson (2007).
[C] Ce^{4+}/Ce^{3+}_{zircon} ratios of zircon $Ce^{4+}$and Ce^{3+}contents are calculated following the method of Ballard et al. (2002) based on the lattice strain model.
[D] log f^a_{O2} and [E]ΔFMQ[b] oxygen fugacity based on zircon are calculated following the method of Smythe and Brenan (2016). ΔFMQ (fayalite-magnetite-quartz) is the log f_{O2} deviation from the FMQ buffer.
[F] log f^a_{O2} and [G]ΔFMQ[b] oxygen fugacity based on zircon are estimated following the method of Loucks et al. (2020).
[H] LREE-I LREE Index are calculated following Bell et al. (2016).

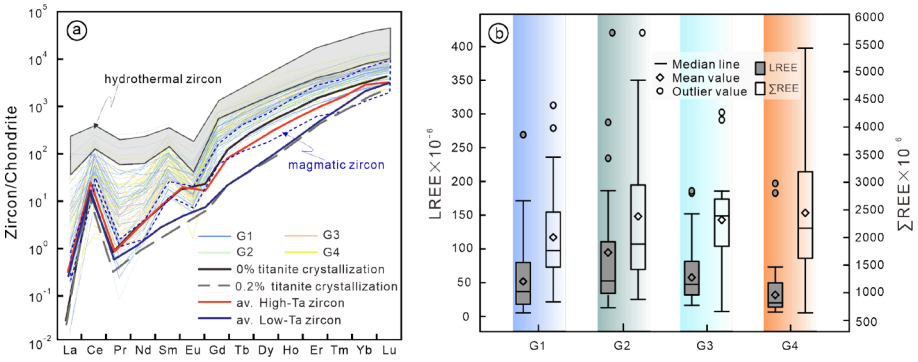

Fig. 6. (a) Chondrite-normalized REE distribution patterns (normalization values from Sun and Mcdonough, 1989) and (b) box plots of LREE and ∑REE contents in zircons from the Kunshan granites. The typical distribution patterns of magmatic and hydrothermal zircons are from Hoskin (2005). Linear REE patterns of 0% titanite crystallization (black solid line), 0.2% titanite crystallization (grey dashed line), average high-Ta zircon (red solid line) and average Low-Ta zircon (blue solid line) are defined by Loader et al. (2017). (For interpretation of the references to colour in this figure legend, the reader is referred to the web version of this article.)

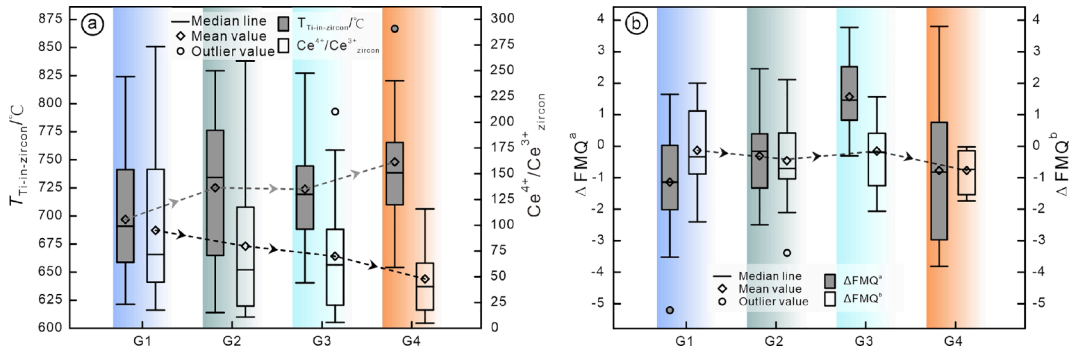

Fig. 7. (a) Box plots of $T_{Ti\text{-}in\text{-}zircon}$, Ce^{4+}/Ce^{3+}_{zircon}; (b) ΔFMQ^a, ΔFMQ^b in zircons from the Kunshan granites; ΔFMQ^a is calculated using the method of Smythe and Brenan (2016), whereas ΔFMQ^b is estimated following the method of Loucks et al. (2020). Note the decreasing trend in the Ce^{4+}/Ce^{3+}_{Zircon} and ΔFMQ^b values from the G1 granite to the G4 granites.

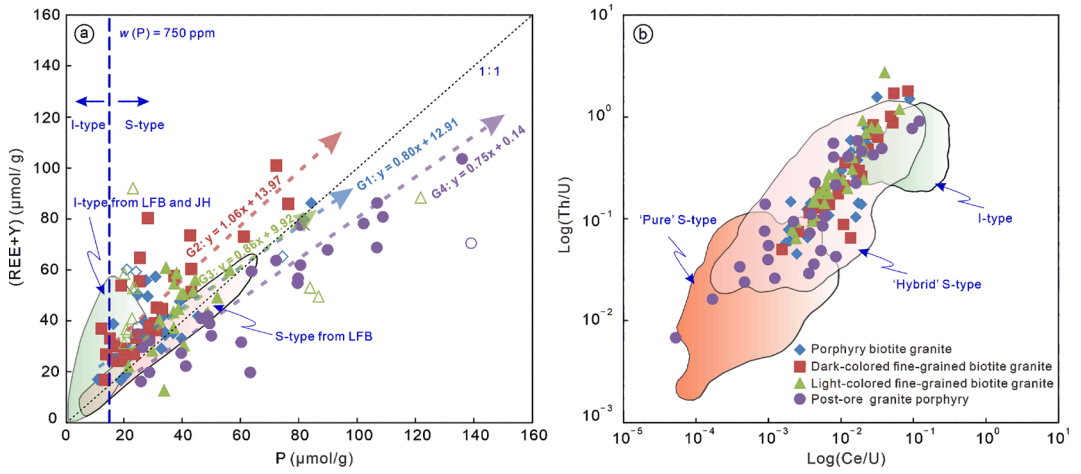

Fig. 8. (a) Relationships between the concentrations of P and ΣREE + Y (μmol/g) in magmatic zircons from the Kunshan granites. The threshold of 750 ppm P for distinguishing between I-type and S-type granites is from (Burnham and Berry, 2017). (b) Ce/U vs. Th/U ratios for magmatic zircons to distinguish I-type, 'hybrid' S-type, and 'pure' S-type granites (Roberts et al., 2024). Reference fields include LFB (Lachlan Fold Belt) and JH (Jack Hills Belt) (Roberts et al., 2024).

those of mantle-derived zircon and lower than those of metasediment-derived zircon; Fig. 9c). This is confirmed by the presence of ancient Proterozoic inherited zircons in the Dahutang granites (Wei et al., 2018; Zhang et al., 2018a). After the initial magmatic stage, substantial crustal assimilation likely occurred between the melt and country rocks as the melt ascended. This assimilation increased the $\delta^{18}O$ value of the melt and disrupted the initial oxygen isotope equilibrium between quartz and early zircon. The re-equilibrium of the oxygen isotopes between quartz and feldspar may reflect this process. The assimilation of high-$\delta^{18}O$ metasediments from the SQSG strata (with an average $\delta^{18}O_{SQSG}$ of + 12.6 ‰, Zhang et al., 1984) resulted in elevated $\delta^{18}O$ values. Under the assumption of a simple mixing model, a 59 % contamination of an average low-$\delta^{18}O$ source composition for I-type-like granite (+9.2 ‰) by SQSG metasediments (+12.6 ‰; Zhang et al., 1984, Fig. 9e) would yield an average $\delta^{18}O$ value of + 11.2 ‰ for the ore-related S-type granite in the Dahutang ore field. This calculation uses the average whole-rock $\delta^{18}O$ value (+11.2 ‰) of fine-grained granite from Peng et al. (2018) as a proxy (Fig. 9d; Text S2). The Pb isotopic data from the Mesozoic ore-related granites fall within the isotopic domain of the SQSG (Ma and Dan, 1996; Zhang et al., 2000; Xiang et al., 2013a; Zhang, 2014; Yu et al., 2021), which is distinct from Neoproterozoic granodiorite regions (Ling et al., 1998) (Fig. 11b). These findings suggest that the Dahutang Mesozoic granites originated from the SQSG metasediments as they lack relationships with Neoproterozoic granodiorite.

The O and Pb isotope data indicate that the Dahutang granites did not originate from a mixture of the SQSG metasediments and Neoproterozoic granodiorite (Wei et al., 2018) or from the mixing of two separate magmas of different chambers with varying proportions of SQSG basic lavas and pelites (Fan et al., 2019). Instead, zircons initially exhibited low $\delta^{18}O$ values, similar to those observed in S-type granitic melts, with substantial contributions from I-type-like source compositions (Fig. 9c). This interpretation is further supported by the Ce/U and Th/U ratios of the zircons, indicating a 'hybrid' S-type granite origin (Fig. 8). Therefore, the S-type granite with low-$\delta^{18}O$ zircon potentially originated from the underlying basement and was characterized by a high proportion of *meta*-igneous rocks. The basement is likely composed of the lower SQSG, which contains substantial *meta*-igneous rocks (Gong et al., 2023). These intercalated *meta*-igneous layers may resemble marine paleo-volcanic eruptive deposits such as the spilite-keratophyres and sandy-argillaceous metasediments. These formations are exposed in the Sheli'ao area of the Pengshan anticline core (Yin et al., 2020, 2024) or in the Dongkou area (pillow basalts), northwestern Jiangxi Province (Xiang et al., 2015b). The preservation of equilibrium $\delta^{18}O$ fractionations between quartz and feldspar, but not between quartz and zircon, in the fine-grained granite supports the hypothesis that contamination by the SQSG metasediments persisted until the *meta*-igneous component in the magma source composition decreased to approximately 41 % (Fig. 10), especially in a protracted magmatic system (e.g., Caracciolo et al., 2022; Itano et al., 2024). The *meta*-igneous-dominated component, constituting 41 % of the total composition, may have significantly contributed to the initial copper supply in the Dahutang ore field (Fig. 10).

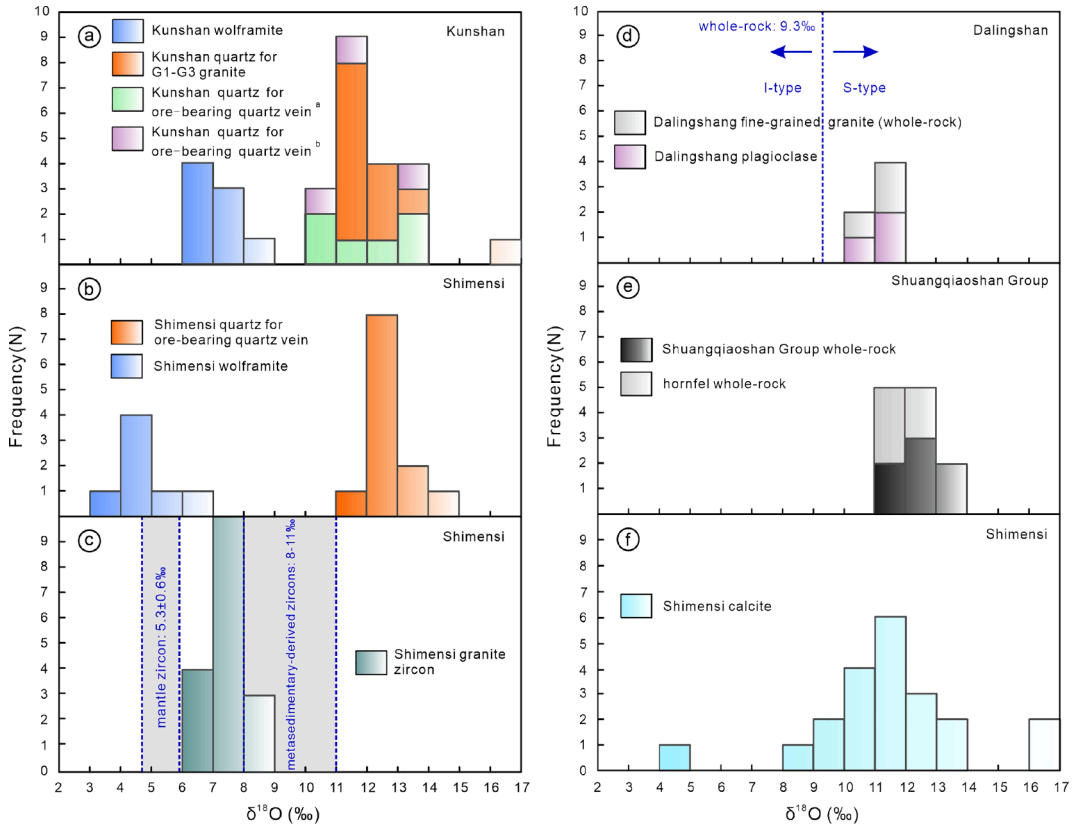

Fig. 9. $\delta^{18}O$ histograms for wolframite and associated minerals from the Kunshan, Shimensi and Dalingshang deposits of the Dahutang ore field. (a) Kunshan quartz from granite and wolframite (this study), ore-bearing quartz vein (Jiang, 2016, Zhang et al., 2018b); (b) Shimensi quartz from quartz-bearing lodes and wolframite (Wang et al., 2015); (c) Shimensi zircon from granite (Wei et al., 2018); (d) Dalingshang fine-grained granite and plagioclase (Peng et al., 2018); (e) whole-rock $\delta^{18}O$ values for the Shuangqiaoshan Group and hornfels (Zhang et al. 1984); (f) Shimensi calcite (Xiang et al., 2013a; Xiang et al., 2013b; Ruan, 2014). Regions of mantle-derived low-$\delta^{18}O$ zircon and metasediment-derived high-$\delta^{18}O$ zircons are after (Valley et al., 1998) and (Kemp et al., 2007), respectively. The $\delta^{18}O$ whole-rock (WR) boundary distinguishing I-type and S-type granites is ca. 9.3‰ (Harris et al., 1997). For details on the $\delta^{18}O$ values see Table S4.

5.1.2. Sources of W-Mo-Cu mineralization

Sulfur isotopes are widely used to identify the origin and evolution of sulfides (Seal, 2006; Johnston, 2011; Pei et al., 2024). In the Kunshan deposit, molybdenite, chalcopyrite and pyrite exhibit $\delta^{34}S$ values ranging from −1.5 ‰ to + 1.5 ‰ (Table S5), suggesting a homogeneous sulfur source. The histogram of $\delta^{34}S$ values for the polymetallic sulfides (Fig. S2) clearly demonstrates isotopic homogeneity and the absence of values within the range of + 1.8 ‰ to + 6.4 ‰, which are typically characteristic of the surrounding SQSG (Huang and Yang, 1990; Zhu and Fan, 1991; Wei, 1996). These findings suggest that the sulfur responsible for the ore formation was isotopically consistent and was derived from deep-seated magmas. The Pb isotopic compositions of Kunshan wolframites were compared with previously reported Pb isotopes from the Shimensi deposit to evaluate the sources of tungsten and the role of country rocks in wolframite precipitation (Table S6; Yu et al., 2021). The Pb isotope data from eight wolframite samples exhibit a linear relationship ($y = 0.4428x - 0.0782$, coefficient of determination $R^2 = 0.9745$; Fig. 11a), indicating a nearly common source of lead.

The Pb isotope evolution diagram (Fig. 11b) shows that five wolframite samples plot in the Pb isotope field of ore-related granites. Three samples are in an area transitional between the Shimensi tungsten and sulfide ores and the Mesozoic ore-related granites, suggesting the coexistence of ore-related granites and tungsten ores. Note that one wolframite sample deviates from the field of ore-related granites and falls within the Pb isotopic domain of the SQSG (Fig. 11b). This indicates that the Pb isotopic composition of Kunshan wolframites is distinct from the relatively purer magma source of the Shimensi wolframite (Fig. 11b). This discrepancy can be explained by the contamination of the Kunshan wolframite by lead from the surrounding SQSG metasediments. The combined S-Pb isotope data and spatial distribution of orebodies hosted in the apical portions of the granite stock (Figs. 3 and 11b, Fig. S2) suggest a genetic linkage between the Kunshan deposit and the underlying granites. The evidence of Pb isotope systematics suggests contamination by the SQSG strata during high-temperature tungsten mineralization.

5.2. Redox conditions of W-Mo-Cu mineralization

5.2.1. Migration of W-Mo-Cu

Unlike Mo and Cu, tungsten combines with oxygen to form tungstate ions ($[WO_4]^{2-}$). Tungsten is a relatively incompatible element with moderate lithophile properties, and it tends to concentrate in residual melts during magma evolution, particularly under reduced conditions of magmatic petrogenesis (Reifenroether et al., 2021). The valence of tungsten is stable as f_{O2} decreases, despite being a variable-valence element (Ertel et al., 1996; Che et al., 2013). Large tungsten-forming granites mainly originate from reductive magmatic systems, such as those of Lake George in Canada (Seal et al., 1987), and of the Zhuxi (Song et al., 2022) and Shimensi deposits (Fan et al., 2019). Reduced W-rich magmas originate from partial melting of supracrustal materials, while oxidized W-rich magmas are derived from partial melting of the lower crust, with additional contributions from mafic magmas (Song et al., 2021, 2023). At lower f_{O2}, tungsten exhibits reduced $D_W^{metal/melt}$, sequestering sufficient tungsten to remain in the melt in its stable form as $[WO_4]^{2-}$ (O'Neill et al., 2008; Trail et al., 2012). The incompatibility of molybdenum increases with increasing f_{O2} level (Lauer and Jones, 1999; Černý et al., 2005). The transport efficiency of Mo and Cu, which are chalcophile elements, is significantly influenced by sulfur species

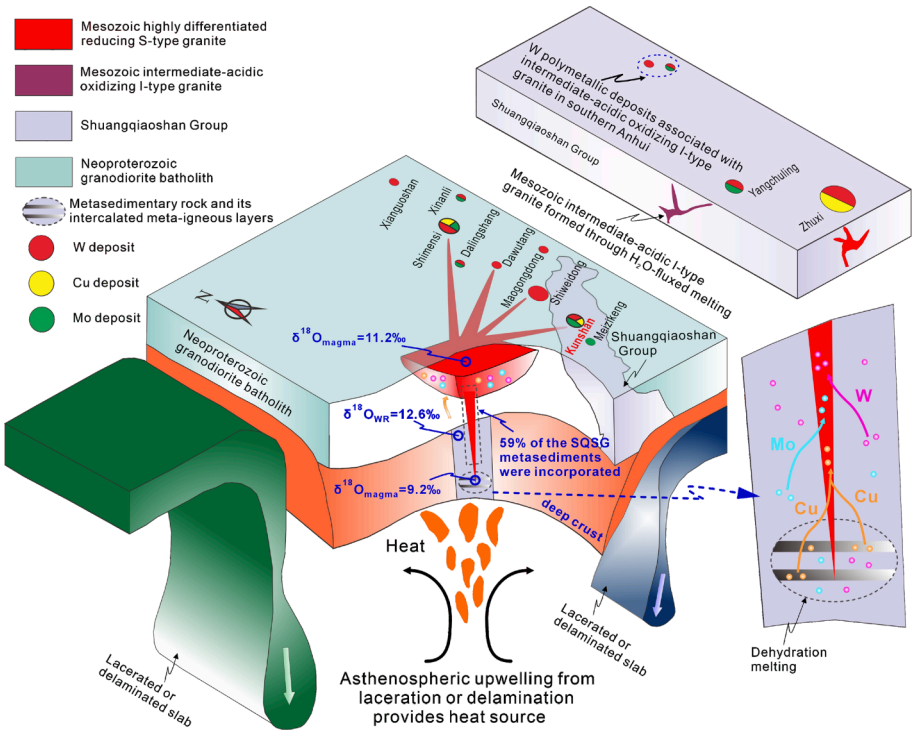

Fig. 10. A metallogenic model of the establishment of the Dahutang tungsten polymetallic ore field and its eastern extensions (modified after Lin et al., 2023). The asthenospheric upwelling caused by lithospheric thickening, delamination or a slab window (Mao et al., 2017), induced dehydration melting of the underlying basement and emplacement of the Mesozoic S-type granites. The melts contained low-$\delta^{18}O$ I-type granitic material and, while ascending to higher crustal levels, they also captured metasedimentary country rocks (with $\delta^{18}O_{magma} = 12.6$ ‰), reducing the low-$\delta^{18}O$ component (with $\delta^{18}O_{magma} = 9.2$ ‰) in the magma source to 41 %. The evolved magma (with $\delta^{18}O_{magma} = 11.2$ ‰) subsequently intruded the country rocks of the Dahutang ore field to form tungsten-bearing polymetallic orebodies. The 41 % *meta*-igneous-dominated component of the magma source likely served as a critical supplier of copper within the Dahutang ore field. WR = whole-rock, SQSG = Shuangqiaoshan Group.

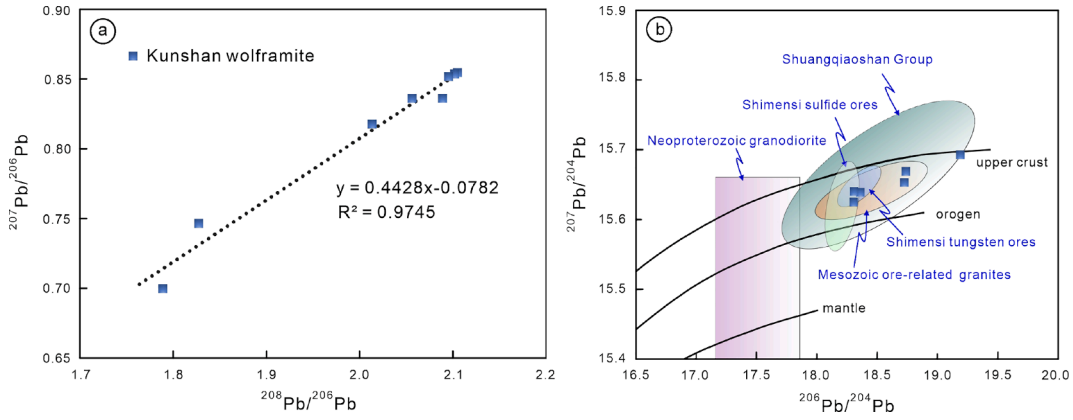

Fig. 11. (a) Lead-isotope evolution diagram showing $^{208}Pb/^{206}Pb$ vs. $^{207}Pb/^{206}Pb$ and (b) $^{206}Pb/^{204}Pb$ vs. $^{207}Pb/^{204}Pb$ for wolframite from the Kunshan deposit. The lead-isotope evolution curves in Figure b are based on Zartman and Doe (1981). Figure b also includes lead isotope fields for the Shuangqiaoshan Group (Ma and Dan, 1996; Zhang et al., 2000), Shimensi tungsten ores (Yu et al., 2021), Mesozoic metallogenic granites, Shimensi sulfide ores (Xiang et al., 2013a; Zhang, 2014; Yu et al., 2021), and the Neoproterozoic granodiorite batholiths in northern Jiangxi and southern Anhui (Ling et al., 1998).

(Sun et al., 2015). In reduced melts, S^{2-} anions and elevated partition coefficients ($D_{Mo}^{sulfide/Si\text{-}melt}$ and $D_{Cu}^{sulfide/Si\text{-}melt}$) suggest that Mo and Cu preferentially bind to divalent sulfur, partition into a sulfide phase, and separate from the melt. Oxidized melts, e.g., magnetite-series granites (Ishihara, 1977), may lose ~ 14 % Mo and ~ 2 % W, while reduced felsic melts, e.g., ilmenite-series granites, likely strip over 90 % of Mo with minimal influence on tungsten (Mengason et al., 2011). Such behavior is observed under high sulfur fugacities and low f_{O2}, as modeled through Rayleigh-fractionation (Mengason et al., 2011).

Zircons from the Kunshan granites were analyzed using the method of (Loucks et al., 2020), and indicate a low f_{O2} environment (Fig. 7b, Fig. S3b). Under reducing conditions, the value of ΔFMQ ranging from −0.55 to −0.20 (Fig. 7b) is approximately two logarithmic units lower than that of typical porphyry Mo-related felsic magma (ΔFMQ ≈ 2; Sun et al., 2015), and the retention of tungsten in a deep source region becomes negligible (Mengason et al., 2011). However, sulfide separation depletes the initial contents of copper and molybdenum, particularly copper, owing to its stronger chalcophile properties compared to those of Mo (Patten et al., 2013). In the Kunshan deposit, the redox state of the magma, characterized by a slightly negative ΔFMQ of −0.55 to −0.20

(Fig. 7b, Fig. S3b), may have facilitated the significant mineralization of tungsten, moderate mineralization of molybdenum and the minor mineralization of copper. This specific f_{O2} range in the early magma during zircon crystallization played a critical role in influencing the migration efficiency of Mo, W and Cu, thereby shaping their ore-forming potential.

5.2.2. Paragenetic W-Mo-Cu mineralization

A robust f_{O2} indicator, which is based on Eu and Ce anomalies, assesses variations in f_{O2} during zircon crystallization, as the differing $D^{zircon/melt}$ values of variable-valence Eu and Ce are sensitive to f_{O2} (Ballard et al., 2002). Caution is necessary when using Eu anomaly to estimate f_{O2}, particularly if titanite co– or pre-crystallized with zircon (Loader et al., 2017). Therefore, it is not feasible to evaluate initial magma's redox conditions solely through Ce and Eu anomalies (Ballard et al., 2002). The zircons from the G1-G4 granites are enriched in Ta and have REE distribution curves above the average curve for high-Ta zircons (Fig. 6a, Loader et al., 2017). The plotted data deviate from the titanite fractionation curve (Fig. S4a), indicating that the co-crystallization of a limited amount of titanite had a negligible influence on the Eu anomalies.

The Eu/Eu* ratios of granites from the Kunshan deposit are comparable with those of the Xihuashan and Shimensi tungsten deposits but are lower than those of the Dexing and Shuikoushan deposits (Zhang et al., 2017; Yang et al., 2018), and higher than those of the Pengshan tin polymetallic deposit (Yin et al., 2024) (Fig. 12). The decreasing trends in the Ce^{4+}/Ce^{3+}_{zircon} ratios and ΔFMQ^{b} values from the G1 to the G4 granites suggest a progressive decline in magma f_{O2} (Fig. 7). This trend and the increasing Hf content and decreasing crystallization temperatures may indicate fractional crystallization (Fig. S4b-c) (Samperton et al., 2015). The G1-G4 granites tend to reduce f_{O2}, and their datasets cluster along trend lines on either side of the distribution patterns (Fig. S4b-c). During fractional crystallization, the f_{O2} of the melts regulated the accumulation of tungsten. As f_{O2} decreases, a lower value of $D_W^{metal/melt}$ facilitates the migration of tungsten and maintains its stable state (O'Neill et al., 2008; Trail et al., 2012). Under low f_{O2} conditions, tungsten exhibits enhanced migration efficiency, whereas variations in sulfur species promote substantial losses of Mo and Cu from deep sources. This effect becomes more pronounced when tungsten is associated with the chalcophile elements Mo and Cu. In the Kunshan deposit, the early stages of magmatism at higher f_{O2} levels likely promoted the extraction of Mo and Cu from the source during melting. In the later stage, under reduced f_{O2} conditions, tungsten migrated efficiently within the highly fractionated melt. Evidence for this is derived from the compositional distinctions between the fine-grained G2 and G3 granites. The G2 granite has relatively high Mo (avg. 10.09 ppm) and Cu (avg. 18.44 ppm) contents, while the subsequent G3 granite contains higher W concentrations (avg. 4.49 ppm).

Although the Kunshan and Shimensi granites experienced similar moderate reduction conditions, the Kunshan deposit is W-Mo-dominated, unlike the W-dominated Shimensi deposit. This divergence may be attributed to the erosion of the quartz vein tungsten orebody (A-zone) at the top of the Kunshan deposit (Fig. 3), leading to the formation of a medium-sized W-Mo-dominated polymetallic deposit. This hypothesis is supported by the spatial distribution of heavy-mineral anomalies in wolframite around the extraction site (Ye et al., 2016). The specific range of magma's f_{O2} is indicative of moderately reducing conditions and is crucial for the origin, migration, accumulation and paragenesis of W-Mo-Cu metals in the Dahutang ore field.

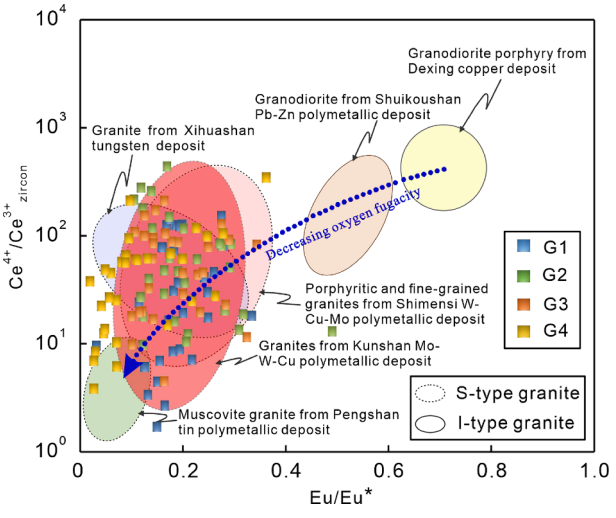

Fig. 12. Plot of zircon Ce^{4+}/Ce^{3+}_{zircon} ratios vs. Eu/Eu* ratios for the Kunshan deposit. Data from additional deposits are included for comparison: granodiorite porphyry from the Dexing copper deposit (Zhang et al., 2017), granodiorite from the Shuikoushan Pb-Zn polymetallic deposit, granite from the Xihuashan tungsten deposit (Yang et al., 2018), porphyritic and fine-grained granites from the Shimensi W-Mo-Cu polymetallic deposit (Sun et al., 2018), and muscovite granite from the Pengshan tin polymetallic deposit (Yin et al., 2024).

5.3. Factors of vertical reverse zoning

5.3.1. Temperatures of equilibrium

Most tungsten polymetallic deposits gradually decrease in mineralization temperature with increasing distance from ore-related granites (Xiang et al., 2015a, 2017; Sun and Chen, 2017). However, the Kunshan deposit exhibits an atypical vertical reverse zoning, with wolframite concentrated at shallow depths and molybdenum and copper concentrated at greater depths (Fig. 3). Such zonation could result from the superposition of multiple parallel episodes of hydrothermal activity or from several sequential stages in the evolution of a single metallogenic system. The Kunshan deposit is characterized by a low water/rock (W/R) ratio, which limits the influence of external fluids (for details see Text S3). As a result, the primary ore-bearing fluids originated from the re-equilibrium of magmatic water, which is consistent with H-O isotopic evidence from fluid inclusions in quartz (Zhang et al., 2018b). The mean temperature of wolframite mineralization in Kunshan (~394°C) is approximately 87 °C higher than that in Shimensi (~307°C) (for details see Text S4). The elevated vapor pressure within the high-temperature system limited the exchange of oxygen isotope between meteoric water and the hydrothermal system responsible for the formation of wolframite.

5.3.2. Composition of country rocks

The country rocks of the epi-metamorphic strata of the Anlelin Formation experienced hornfelsization due to magmatic heating, which led to the fractionation of approximately 0.8 ‰ oxygen isotopes. The average values of $\delta^{18}O$ for hornfels and epi-metamorphic rocks of the Anlelin Formation are + 11.8 ‰ and + 12.6 ‰, respectively (Fig. 9b; Zhang et al., 1984) suggesting that a portion of the high-$\delta^{18}O$ material of the Anlelin Formation arrived at the wolframite metallogenic hydrothermal system through contamination, but not by mixing of fluid with meteoric water. This interpretation is supported by the consistent oxygen isotopic compositions of quartz in wolframite-bearing quartz veins and in the G1-G3 granites (Text S3). More evidence comes from the Pb isotopic signatures of wolframite. One wolframite sample shows a lead isotopic value that deviates from those of the ore-related granite but falls within the Pb isotopic range of the SQSG (Fig. 11b). In contrast, the Shimensi deposit formed under a different scenario, within a closed system, located in an unidirectionally solidified pegmatoid stockscheider, which formed at the interface between the granite stock and wallrock granodiorite (Xiang et al., 2017). The closed-system conditions resulted in negligible isotopic exchange during the wolframite-quartz stage, as demonstrated by the lead isotopic data of Shimensi wolframite that fall within the Pb isotopic range of the Mesozoic granites

(Fig. 11b). Thus, the mineralization in the Kunshan deposit formed due to the interaction of fluids with tungsten leached from crystallized ore-related granites. The efficient transportation of the fluids was favored by the structures of stratification, foliation, and joint networks well developed in the sedimentary rocks of the Anlelin Formation.

Breccia-type orebodies in the apical parts of granitic bodies are present in the Shimensi deposit but are absent in the Kunshan deposit due to the lack of a crypto-explosion structure. Unlike the Shimensi deposit, which lacks joint networks in the Neoproterozoic granodiorite country rocks, the fluids of the Kunshan deposit enriched in F, S and ore-forming constituents, were concentrated in low-pressure zones atop the granite. Once the hydrostatic pressure of those fluids exceeded the lithostatic pressure, the high-temperature ore-bearing fluids rapidly migrated towards the distal A- and B- zones through the sub-vertical foliation (Fig. 13a, b). Thermodynamic experiments have shown that a gaseous hydrate of tungsten has a relatively high hydration coefficient (2.9) at ~ 400 °C to promote its migration towards the apical parts of granite bodies (Zhang and Chen, 2015). The migrating fluids filled the fractures and weak zones and triggered the formation of quartz-wolframite veins with elevated $\delta^{18}O_{wof}$ values (avg. + 7.1 ‰) at high temperatures (~ 394 °C, Text S4). The hornfelsized country rocks were encapsulated by wolframite-bearing quartz veins at + 1020 m high levels in the fracture system (Fig. 13b). Consequently, wolframite hosted at higher elevations exhibited elevated $\delta^{18}O_{wof}$ values and higher metallogenic temperatures (~394 °C; Fig. S5), reflecting the preferential migration of tungsten-rich volatile complexes toward the upper sections of the fracture system. At the middle to lower parts of the fracture system, the conditions were lower-temperatures and more reduced to provide the metal sulfide mineralization in the C- and D- zones (Fig. 13c). The Mo mineralization partially overlapped with the early-stage W mineralization but stopped before the mineralization of Cu started. This overlap enabled the widespread dissemination of molybdenum, driven by the gradual descent of the thermal center of the ore-forming fluid and the formation of vertical reverse zoning with the copper orebody beneath the shallow tungsten orebody (Fig. 13c). The vertical reverse zoning in the Kunshan deposit suggests that the precipitation of ore-forming elements is governed by the separation modes of the ore-bearing fluids (void filling or permeability replacement) from parental magmas and the physical properties of the country rocks, compact vs. sheared/fissured, within the metallogenic system during W-Mo-Cu mineralization. In open metallogenic systems, under low-pressure conditions, volatile-rich tungsten-bearing fluids can migrate over a distance of more than 500 m from ore-related granitic intuitions due to "retrograde solubility" (Liu et al., 2024). In the Kunshan deposit, volatile-rich fluids (Fig. 2f) and the open metallogenic system were key factors in the vertical reverse zoning of ore mineralization. For example, despite similar geological characteristics, there is no reverse zoning and no tungsten mineralization in the neighboring Meizikeng molybdenum deposit (Fig. 10) because of the lack of highly volatile components in its ore-forming fluid (Zhang et al., 2013). In contrast, vertical reverse zoning of metals is observed in the Xingluokeng (northern Fujian), Meiziwo (Guangdong), and Pangushan and Huangsha (southern Jiangxi) quartz-vein-type tungsten deposits. The fractures in these deposits formed during or prior to mineralization, thereby providing open pathways for the migration of ore-forming fluids (Xia et al., 1981; Cai, 1984; Ren et al., 1986; Chen and Zhang, 2005). In such circumstances, exploration and exploitation efforts should be sustained despite the decrease in tungsten ore grade and the increase in metal sulfide grade with depth. Quartz vein-type tungsten polymetallic deposits, which are characterized by abundant volatiles and open systems, may host late-stage Cu (Mo ± Ag) mineralization at deeper levels beneath tungsten orebodies or near the contact interface between granitic intrusions and country rocks, such as those in the Zhangdongkeng deposit in southern Jiangxi and the Meiziwo in northern Guangdong (Chen and Zhang, 2005; Xing et al., 2010).

6. Conclusions

The target of our research was the Kunshan W-Mo-Cu deposit located in the world-class Dahutang tungsten ore district in the middle segment of the Jiangnan Orogen, South China. Our comprehensive analysis of the geological structure of the deposit, in-situ elemental and U-Pb isotopic compositions of zircons, coupled with stable and radioactive isotope studies of minerals from diverse mineralization stages and ore-related granites, provides robust evidence about the hybrid sources of Mesozoic intrusions, highlights the role of f_{O2} in the migration of W-Mo-Cu, enhances the understanding of the paragenetic mechanism of W-Mo-Cu mineralization, and sheds light on the processes driving vertical reverse zoning mineralization.

The ore-related fine-grained granite in the Dahutang ore field experienced contamination from overlying metasediments until the *meta*-igneous-dominated component (with $\delta^{18}O_{magma}$ = 9.2 ‰) in the magma source composition decreased to 41 % and thus provided the initial supply of copper. The Kunshan W-Mo-Cu mineralization is closely

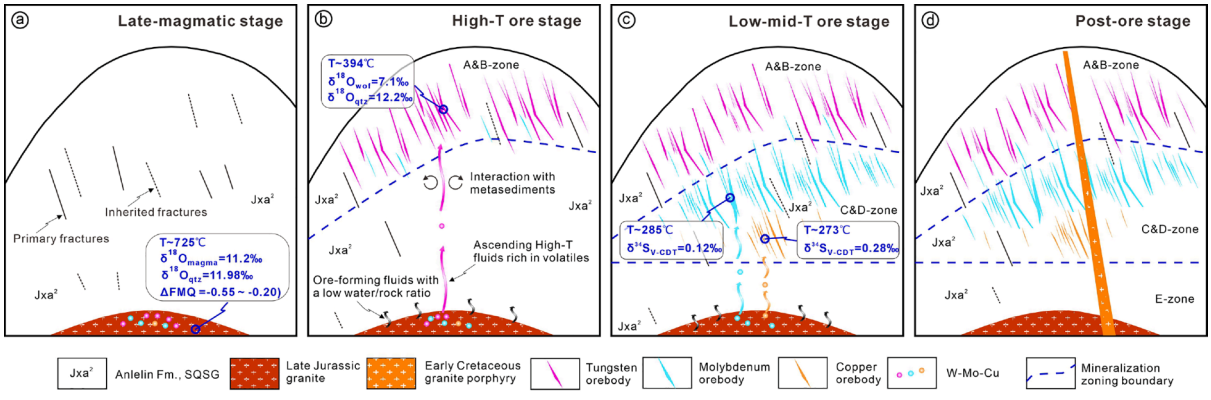

Fig. 13. Model of vertical reverse zoning in the Kunshan W-Mo-Cu polymetallic deposit. (a) Source extraction and conduit formation: W-Mo-Cu ore-forming elements were extracted from the source region by moderately reduced magma; Primary and inherited fractures established an open metallogenic system, providing well-developed conduits for fluid migration. (b) High-temperature fluid migration: High-temperature (~394 °C) W-rich fluids, characterized by robust 'penetrative capabilities' and high volatile content, preferentially migrated to the upper parts of the fractures within an open metallogenic system (Zhang and Chen, 2015; Liu et al., 2024); Interactions between ore-forming fluids and metasediments induced high $\delta^{18}O$ values and a wide range of Pb isotopic compositions in wolframite. (c) Low- to moderate-temperature mineralization: Mo-Cu-rich fluids, at low to moderate temperatures (~280 °C; Zhang et al., 2018b), mineralized beneath the high-temperature (~394 °C) tungsten orebodies, forming a vertical reverse zoning pattern. (d) Post-mineralization intrusion: Granite porphyry dikes cut through the ore-forming granites and polymetallic orebodies, marking the end of diagenesis and mineralization in the Kunshan deposit.

associated with the underlying granites, with evidence of contamination from overlying strata during high-temperature W mineralization. The magma redox state (ΔFMQ = -0.55 ~ -0.20) played a pivotal role in the origin, migration, accumulation, and paragenesis of W-Mo-Cu metals, and provided favorable conditions for rich tungsten mineralization, moderate molybdenum and minor copper mineralization. High-temperature (~394 °C), volatile-rich fluids possessing string 'penetrative capabilities' drove the vertical reverse zoning of mineralization in an open metallogenic system.

CRediT authorship contribution statement

Qingqing Yin: Writing – review & editing, Writing – original draft, Resources, Methodology, Investigation, Formal analysis, Data curation, Conceptualization. **Juxing Tang:** Writing – review & editing, Writing – original draft, Supervision, Data curation, Conceptualization. **Qiuming Pei:** Writing – review & editing, Data curation, Conceptualization. **Inna Safonova:** Writing – review & editing, Conceptualization. **Xinkui Xiang:** Writing – review & editing, Resources, Investigation, Conceptualization. **Jingjing Dai:** Writing – review & editing. **Aorigele Zhou:** Writing – review & editing. **Bin Lin:** Writing – review & editing, Validation, Methodology. **Yumin Xu:** Writing – review & editing, Visualization, Software, Investigation. **Zhendong Yu:** Visualization. **Jinling Xie:** Writing – review & editing, Software, Resources, Investigation. **Ruihua Lin:** Writing – review & editing, Software, Investigation. **Bo Peng:** Writing – review & editing, Visualization, Methodology, Investigation. **Liqiang Wang:** Writing – review & editing, Visualization, Funding acquisition.

Acknowledgments

We extend our gratitude to Shao-Zhen Ye, Rong Tan, and Xian-Jun Zhou from the Jiangxi Bureau of Geology for their invaluable assistance during our field investigation. We also appreciate the support and guidance provided by Prof. Tao-Fa Zhou, Prof. Quan-Zhong Li, and Eng. Mu Liu during the laboratory work. Special thanks are extended to Prof. Xian-Guang Wang for their constructive suggestions, which significantly enhanced this study. This research was financially supported by the National Key R & D Program of China (2021YFC2900100 and 2022YFC2905003), the National Natural Science Foundation of China (42302104), the Ministry of Science and Higher Education of Russia, State Assignment Project (122041400044-2), the National Science and Technology Award Reserve Project Cultivation Plan from the Science and Technology Department of Jiangxi Province (20203AEI91004) and the Technology Innovation Guidance Project of Science and Technology Department of Jiangxi Province (S2023KJSLG0007).

Appendix A. Supplementary data

Supplementary data to this article can be found online at https://doi.org/10.1016/j.gr.2025.03.004.

References

Ballard, J.R., Palin, M.J., Campbell, I.H., 2002. Relative oxidation states of magmas inferred from Ce (IV)/Ce (III) in zircon: application to porphyry copper deposits of northern Chile. Contributions Mineral. Petrol. 144, 347–364. https://doi.org/10.1007/s00410-002-0402-5.

Bell, E.A., Boehnke, P., Harrison, T.M., 2016. Recovering the primary geochemistry of Jack Hills zircons through quantitative estimates of chemical alteration. Geochimica Cosmochim. Acta. 191, 187–202. https://doi.org/10.1016/j.gca.2016.07.004.

Burnham, A.D., Berry, A.J., 2012. An experimental study of trace element partitioning between zircon and melt as a function of oxygen fugacity. Geochimica Cosmochim. Acta. 95, 196–212. https://doi.org/10.1016/j.gca.2012.07.034.

Burnham, A.D., Berry, A.J., 2017. Formation of Hadean Granites by Melting of Igneous Crust: Nature Geosci. 10, 457–461. https://doi.org/10.1016/j.gca.2012.07.028.

Cai, Y.L., 1984. A study of the genetic type of Xingluokeng tungsten (molybdenum) deposit. Fujian Province. Mineral Depos. 1, 27–36 [in Chinese with English abstract].

Caracciolo, A., Halldórsson, S.A., Bali, E., Marshall, E.W., Jeon, H., Whitehouse, M.J., Barnes, J.D., Guðfinnsson, G.H., Kahl, M., Hartley, M.E., 2022. Oxygen isotope evidence for progressively assimilating trans-crustal magma plumbing systems in Iceland. Geology 50, 796–800. https://doi.org/10.1130/G49874.1.

Černý, P., Blevin, P.L., Cuney, M., London, D., 2005. Granite-related ore deposits: Michel and London. Economic Geology 100th Anniversary. Society of Economic Geologists. 337–370. https://doi.org/10.5382/AV100.12.

Che, X.D., Linnen, R.L., Wang, R.C., Aseri, A., Thibault, Y., 2013. Tungsten solubility in evolved granitic melts: an evaluation of magmatic wolframite. Geochimica Cosmochim. Acta. 106, 84–98. https://doi.org/10.1016/j.gca.2012.12.002.

Chen, S.X., Zhang, F.L., 2005. The metallogenic regularity of silver deposits in northern Guangdong. West-China Explor. Eng. 17, 80–82. https://doi.org/10.3969/j.issn.1004-5716.2005.12.040 [in Chinese].

Cherniak, D.J., Watson, E.B., 2003. Diffusion in Zircon. Reviews Mineral. Geochem. 53, 113–143. https://doi.org/10.2113/0530113.

Claiborne, L.L., Miller, C.F., Wooden, J.L., 2010. Trace element composition of igneous zircon: a thermal and compositional record of the accumulation and evolution of a large silicic batholith, Spirit Mountain. Nevada. Contributions Mineral. Petrol. 160, 511–531. https://doi.org/10.1007/s00410-010-0491-5.

Ertel, W., O'Neill, H.S.C., Dingwell, D.B., Spettel, B., 1996. Solubility of tungsten in a haplobasaltic melt as a function of temperature and oxygen fugacity. Geochimica Cosmochim. Acta 60, 1171–1180. https://doi.org/10.1016/0016-7037(96)00022-1.

Fan, X.K., Mavrogenes, J., Hou, Z.Q., Zhang, Z.Y., Wu, X., Dai, J., 2019. Petrogenesis and metallogenic significance of multistage granites in Shimensi tungsten polymetallic deposit, Dahutang giant ore district, South China. Lithos 336, 326–344. https://doi.org/10.1016/j.lithos.2019.04.001.

Ferry, J.M., Watson, E.B., 2007. New thermodynamic models and revised calibrations for the Ti-in-zircon and Zr-in-rutile thermometers. Contributions Mineral. Petrol. 154, 429–437. https://doi.org/10.1007/s00410-007-0201-0.

Giletti, B.J., 1986. Diffusion effects on oxygen isotope temperatures of slowly cooled igneous and metamorphic rocks. Earth Planet. Sci. Lett. 77, 218–228. https://doi.org/10.1016/0012-821X(86)90162-7.

Gong, M., Wu, J.H., Ji, H., Xu, M.L., Kuang, E.L., Jiang, B.L., Li, G.M., Li, Y.J., 2023. Occurrence of lithium and geochronology of magmatism and mineralization in Dagang granite-associated lithium deposit, west Jiangxi province. Earth Sci. 48, 4370–4386 [in Chinese with English abstract]. doi: 10.3799/dqkx.2023.193.

Harris, C., Faure, K., Diamond, R.E., Scheepers, R., 1997. Oxygen and hydrogen isotope geochemistry of S-and I-type granitoids: the Cape granite suite. South Africa. Chemical Geol. 143, 95–114. https://doi.org/10.1016/S0009-2541(97)00103-4.

Hoskin, P.W.O., 2005. Trace-element composition of hydrothermal zircon and the alteration of Hadean zircon from the Jack Hills. Australia. Geochimica Cosmochim. Acta 69, 637–648. https://doi.org/10.1016/j.gca.2004.07.006.

Hoskin, P.W., 2000. Patterns of chaos: fractal statistics and the oscillatory chemistry of zircon. Geochimica Cosmochim. Acta 64, 1905–1923. https://doi.org/10.1016/S0016-7037(00)00330-6.

Huang, H.L., Yang, W.S., 1990. Geological characteristics and genesis of Jinshan gold deposit in the northeastern Jiangxi province. Contributions Geol. Miner. Resour. Res. 5, 29–39 [in Chinese with English abstract].

Irber, W., 1999. The lanthanide tetrad effect and its correlation with K/Rb, Eu/Eu*, Sr/Eu, Y/Ho, and Zr/Hf of evolving peraluminous granite suites. Geochimica Cosmochim. Acta 63, 489–508. https://doi.org/10.1016/S0016-7037(99)00027-7.

Ishihara, S., 1977. The magnetite-series and ilmenite-series granitic rocks. Min. Geol. 27, 293–305.

Itano, K., Takehara, M., Horie, K., Iizuka, T., Nishio, I., Morishita, T., 2024. A long-lived mafic magma reservoir: zircon evidence from a hornblende peridotite in the Hida belt, Japan. Geology 52, 3–6. https://doi.org/10.1130/G51560.1.

Jiang, C.Q., 2016. The research on the geochemical characteristics and genesis of the Dawutang tungsten polymetallic deposit in Jiangxi [MA thesis]. University of Technology, Nanchang, East China, 75p [in Chinese with English abstract].

Johnston, D.T., 2011. Multiple sulfur isotopes and the evolution of earth's surface sulfur cycle. Earth-Sci. Rev. 106, 161–183. https://doi.org/10.1016/j.earscirev.2011.02.003.

Kemp, A., Hawkesworth, C.J., Foster, G.L., Paterson, B.A., Woodhead, J.D., Hergt, J.M., Gray, C.M., Whitehouse, M.J., 2007. Magmatic and crustal differentiation history of granitic rocks from Hf-O isotopes in zircon. Science 315, 980–983. https://doi.org/10.1126/science:1136154.

Keyser, W., Müller, A., Knoll, T., Menuge, J.F., Steiner, R., Berndt, J., Hart, E., Fegan, T., Harrop, J., 2023. Quartz chemistry of lithium pegmatites and its petrogenetic and economic implications: examples from Wolfsberg (Austria) and Moylisha (Ireland). Chemical Geol. 630, 121507. https://doi.org/10.1016/j.chemgeo.2023.121507.

Lauer Jr, H.V., Jones, J.H., 1999. Tungsten and nickel partitioning between solid and liquid metal; Implications for high-pressure metal/silicate experiments. Lunar and Planetary Science Conference, 1617.

Li X.H., Li W.X., Li Z.X., 2007. Further discussion on the genetic types and tectonic significance of the early Yanshanian granites in Nanling. China Sci. Bull. 52(009), 981-991 [in Chinese]. https://doi.10.3321/j.issn:0023-074X.2007.09.001.

Lin, B., Tang, J.X., Tang, P., Beaudoin, G., Laflamme, C., Li, F.Q., Zheng, W.B., Song, Y., Qi, J., Sun, M., Cao, H.W., Leng, Q.F., Zhou, G.L., Zou, B., Corey, J.W., Yang, C., 2024. Multi-pulsed magmatism and duration of the hydrothermal system of the giant Jiama porphyry Cu system. Tibet. China. Economic Geol. 119, 201–217. https://doi.org/10.5382/econgeo.5054.

Lin, R.H., Yin, Q.Q., Xiang, X.K., Liang, F., Yang, X.F., Wang, T.C., Liu, H.Q., Zhou, W.J., Zhu, B., 2023. Molybdenite Re-Os isotopic age of the Kunshan Mo-W-Cu polymetallic deposit in the Jiangxi Province and its evolution of metallogenic geodynamics. Geology China 50, 1176–1187. https://doi.org/10.12029/gc20200115001 [in Chinese with English abstract].

Ling, H.F., Xu, S.J., Shen, W.Z., Wang, R.C., Lin, Y.P., 1998. Nd, Sr, Pb and O isotopic compositions of late Proterozoic Gezong- and Donggu-granites in the west margin of Yangtze Plate and comparison with other coeval granitoids. Acta Petrol. Sin. 14, 269–277 [in Chinese with English abstract]. doi: 10.3969/j.issn.1000-0569.1998.03.001.

Liu, H., Liu, X.C., Zhang, D.H., Zhou, Z.J., Han, F.B., 2024. The precipitation mechanisms of scheelite from CO_2-rich hydrothermal fluids: Insight from thermodynamic modeling. Applied Geochem. 175, 106187. https://doi.org/10.1016/j.apgeochem.2024.106187.

Liu, Y.S., Hu, Z., Gao, S., Günther, D., Xu, J., Gao, C., Chen, H., 2008. In situ analysis of major and trace elements of anhydrous minerals by LA-ICP-MS without applying an internal standard. Chemical Geol. 257, 34–43. https://doi.org/10.1016/j.chemgeo.2008.08.004.

Loader, M.A., Nathwani, C.L., Wilkinson, J.J., Armstrong, R.N., 2022. Controls on the magnitude of Ce anomalies in zircon. Geochimica Cosmochim. Acta 328, 242–257. https://doi.org/10.1016/j.gca.2022.03.024.

Loader, M.A., Wilkinson, J.J., Armstrong, R.N., 2017. The effect of titanite crystallisation on Eu and Ce anomalies in zircon and its implications for the assessment of porphyry Cu deposit fertility. Earth Planet. Sci. Lett. 472, 107–119. https://doi.org/10.1016/j.epsl.2017.05.010.

Loucks, R.R., Fiorentini, M.L., Henríquez, G.J., 2020. New magmatic oxybarometer using trace elements in zircon. Journal Petrol. 61, egaa034. https://doi.org/10.1093/petrology/egaa034.

Ma, Z.D., Dan, G.X., 1996. The background of regional lead isotopic compositions and their application in the lower and middle reaches of the Yangtze River and neighboring areas. Acta Geol. Sin. 70, 324–334. https://doi.org/10.19762/j.cnki.dizhixuebao.1996.04.005.

Mao, J.W., Wu, S.H., Song, S.W., Dai, P., Xie, G.Q., Su, Q.W., Liu, P.P., Wang, X.G., Yu, Z. Z., Chen, X.Y., Tang, W.X., 2020. The world-class Jiangnan tungsten belt: Geological characteristics, metallogeny, and ore deposit model. China Sci. Bull. 65, 3746–3762 [in Chinese with English abstract]. doi: 10.1360/TB-2020-0370.

Mao, J.W., Xiong, B.K., Liu, J., Pirajno, F., Cheng, Y., Ye, H., Song, S., Dai, P., 2017. Molybdenite Re/Os dating, zircon U-Pb age and geochemistry of granitoids in the Yangchuling porphyry W-Mo deposit (Jiangnan tungsten ore belt), China: implications for petrogenesis, mineralization and geodynamic setting. Lithos 286, 35–52. https://doi.org/10.1016/j.lithos.2017.05.023.

Mao, Z.H., Cheng, Y., Liu, J., Yuan, S., Wu, S., Xiang, X., Luo, X., 2013. Geology and molybdenite Re-Os age of the Dahutang granite-related veinlets-disseminated tungsten ore district in the Jiangxi province, China: Ore Geol. Rev. 53, 422–433. https://doi.org/10.1016/j.oregeorev.2013.02.005.

Mengason, M.J., Candela, P.A., Piccoli, P.M., 2011. Molybdenum, tungsten and manganese partitioning in the system pyrrhotite-Fe-S-O melt-rhyolite melt: impact of sulfide segregation on arc magma evolution. Geochimica Cosmochim. Acta 75, 7018–7030. https://doi.org/10.1016/j.gca.2011.08.042.

O'Neill, H.S.C., Berry, A.J., Eggins, S.M., 2008. The solubility and oxidation state of tungsten in silicate melts: Implications for the comparative chemistry of W and Mo in planetary differentiation processes. Chemical Geol. 255, 346–359. https://doi.org/10.1016/j.chemgeo.2008.07.005.

Patten, C., Barnes, S., Mathez, E.A., Jenner, F.E., 2013. Partition coefficients of chalcophile elements between sulfide and silicate melts and the early crystallization history of sulfide liquid: LA-ICP-MS analysis of MORB sulfide droplets. Chemical Geol. 358, 170–188. https://doi.org/10.1016/j.chemgeo.2013.08.040.

Pei, Q.M., Li, C.H., Ma, S.B., Liang, Y., Cao, H.W., Ge, H.F., Shen, J.L., Safonova, I., 2024. A rare sellaite-bearing orogenic gold deposit at Pianyanzi, Yangtze Craton: Ore genesis as implied from in-situ studies of pyrite. Ore Geol. Rev. 165, 105866. https://doi.org/10.1016/j.oregeorev.2023.105866.

Peng, N.J., Jiang, S.Y., Xiong, S.F., Pi, D.H., 2018. Fluid evolution and ore genesis of the Dalingshang deposit, Dahutang W-Cu ore district, northern Jiangxi province. South China. Mineralium Depos. 53, 1079–1094. https://doi.org/10.1007/s00126-018-0796-2.

Pirkle, F.L., Podmeyer, D.A., 1993. Zircon: origin and uses. Transactions 292, 1–20.

Reifenroether, R., Muenker, C., Scheibner, B., 2021. Evidence for Tungsten Mobility during Oceanic Crust Alteration: Chemical Geol. 584, 120504. https://doi.org/10.1016/j.chemgeo.2021.120504.

Ren, Y.C., Cheng, M.Q., Wang, C.C., 1986. Characteristics and vertical zoning of tungsten-bismuth minerals in the Pangushan quartz-vein type tungsten deposit of Jiangxi province. Mineral Depos. 2, 65–76 [in Chinese with English abstract].

Roberts, N.M., Yakymchuk, C., Spencer, C.J., Keller, C.B., Tapster, S.R., 2024. Revisiting the discrimination and distribution of S-type granites from zircon trace element composition. Earth Planet. Sci. Lett. 633, 118638. https://doi.org/10.1016/j.epsl.2024.118638.

Ruan, K., 2014. Geochemical characteristics and ore genesis of Shimensi tungsten deposit in Dahutang [MA thesis]. Nanchang, East China University of Technology, 74p [in Chinese with English abstract].

Samperton, K.M., Schoene, B., Cottle, J.M., Keller, C.B., Crowley, J.L., Schmitz, M.D., 2015. Magma emplacement, differentiation and cooling in the middle crust: integrated zircon geochronological-geochemical constraints from the Bergell intrusion, central alps. Chemical Geol. 417, 22–340. https://doi.org/10.1016/j.chemgeo.2015.10.024.

Seal, R.R., 2006. Sulfur isotope geochemistry of sulfide minerals. Reviews Mineral. Geochem. 61, 633–677. https://doi.org/10.2138/rmg.2006.61.12.

Seal, R.R., Clark, A.H., Morrissy, C.J., 1987. Stockwork tungsten (scheelite)-molybdenum mineralization, Lake George, southwestern New Brunswick. Economic Geol. 82, 1259–1282. https://doi.org/10.2113/gsecongeo.82.5.1259.

Smythe, D.J., Brenan, J.M., 2015. Cerium oxidation state in silicate melts: combined fO_2, temperature and compositional effects. Geochimica Cosmochim. Acta 170, 173–187. https://doi.org/10.1016/j.gca.2015.07.016.

Smythe, D.J., Brenan, J.M., 2016. Magmatic oxygen fugacity estimated using zircon-melt partitioning of cerium. Earth Planet. Sci. Lett. 453, 60–266. https://doi.org/10.1016/j.epsl.2016.08.013.

Song, S.W., Mao, J.W., Xie, G., Su, Q., Jian, W., Ouyang, Y.P., 2022. Deciphering deep-seated, highly fractionated, and reduced granitic magma systems associated with world-class scheelite skarn ores: a case study of the Zhuxi deposit. South China. Ore Geol. Rev. 149, 105084. https://doi.org/10.1016/j.oregeorev.2022.105084.

Song, S.W., Mao, J.W., Xie, G.Q., Lehmann, B., Jian, W., Wang, X.G., 2021. The world-class mid-Mesozoic Jiangnan tungsten belt, South China: Coeval large reduced and small oxidized tungsten systems controlled by different magmatic petrogeneses. Ore Geol. Rev. 139, 104543. https://doi.org/10.1016/j.oregeorev.2021.104543.

Song, W.L., Yao, J.M., Chen, H., Sun, W., Lai, C., Xiang, X.K., Luo, X., Jourdan, F., 2018. A 20 m.y. Long-lived successive mineralization in the giant Dahutang W-Cu-Mo deposit. South China. Ore Geol. Rev. 95, 401–407. https://doi.org/10.1016/j.oregeorev.2018.02.033.

Sun, K.K., Chen, B., 2017. Trace elements and Sr-Nd isotopes of scheelite: implications for the W-Cu-Mo polymetallic mineralization of the Shimensi deposit. South China. American Mineral. 102, 1114–1128. https://doi.org/10.2138/am-2017-5654.

Sun, K.K., Chen, B., Deng, J., Ma, X., 2018. Source of copper in the giant Shimensi W-Cu-Mo polymetallic deposit, South China: constraints from chalcopyrite geochemistry and oxygen fugacity of ore-related granites. Ore Geol. Rev. 101, 919–935. https://doi.org/10.1016/j.oregeorev.2018.08.029.

Sun, S., Mcdonough, W.F., 1989. Chemical and isotopic systematics of oceanic basalts: implications for mantle composition and processes. Geological Society, London, Special Publications 42, 313–345. https://doi.org/10.1144/GSL.SP.1989.042.01.19.

Sun, W.D., Huang, R.F., Li, H., Hu, Y., Zhang, C., Sun, S., Zhang, L., Ding, X., Li, C., Zartman, R.E., 2015. Porphyry deposits and oxidized magmas. Ore Geol. Rev. 65, 97–131. https://doi.org/10.1016/j.oregeorev.2014.09.004.

Trail, D., Bindeman, I.N., Watson, E.B., Schmitt, A.K., 2009. Experimental calibration of oxygen isotope fractionation between quartz and zircon. Geochimica Cosmochim. Acta 73, 7110–7126. https://doi.org/10.1016/j.gca.2009.08.024.

Trail, D., Watson, E.B., Tailby, N.D., 2012. Ce and Eu anomalies in zircon as proxies for the oxidation state of magmas. Geochimica Cosmochim. Acta 97, 70–87. https://doi.org/10.1016/j.gca.2012.08.032.

Valley, J.W., Kinny, P.D., Schulze, D.J., Spicuzza, M.J., 1998. Zircon megacrysts from kimberlite: oxygen isotope variability among mantle melts. Contributions Mineral. Petrol. 133, 1–11. https://doi.org/10.1007/s004100050432.

Vermeesch, P., 2018. Isoplot R: a free and open toolbox for geochronology. Geoscience Front. 9, 1479–1493. https://doi.org/10.1016/j.gsf.2018.04.001.

Wang, H., Feng, C.Y., Li, D.X., Xiang, X.K., Zhou, J.H., 2015. Sources of granitoids and ore-forming materials of Dahutang tungsten deposit in northern Jiangxi Province: Constraints from mineralogy and isotopic tracing. Acta Petrol. Sin. 31, 725–739 [in Chinese with English abstract].

Wang, X.G., Cao, S.H., Gong, L.X., Hu, Z.H., Cao, M.X., Zhang, D.H., Chen, Q.R., 2023. Tungsten-tin polymetallic metallogenic series and prospecting in Jiangxi Province. Acta Geosci. Sin. 44, 916–932. https://doi.org/10.3975/cagsb:2022.112301.

Wei, W.F., Shen, N., Yan, B., Lai, C., Yang, J., Gao, W., Liang, F., 2018. Petrogenesis of ore-forming granites with implications for W-mineralization in the super-large Shimensi tungsten-dominated polymetallic deposit in northern Jiangxi province. South China. Ore Geol. Rev. 95, 1123–1139. https://doi.org/10.1016/j.oregeorev.2017.12.022.

Wei, X.L., 1996. Geological characteristics of Jinshan ductile shear zone-type gold deposit in Jiangxi. Geology Jiangxi 10, 52–64 [in Chinese with English abstract].

Whitehouse, M.J., Kamber, B.S., 2002. On the overabundance of light rare earth elements in terrestrial zircons and its implication for earth's earliest magmatic differentiation. Earth Planet. Sci. Lett. 204, 333–346. https://doi.org/10.1016/s0012-821x(02)01000-2.

Xia, H.Y., Liang, S.Y., Shuai, D.Q., 1981. Fluorite characteristics and metallogenic distribution of the Huangsha vein tungsten deposit in southern Jiangxi. Mineralogy Petrol. 1, 112–118 [in Chinese with English abstract].

Xiang, X.K., 2012. Metallogenic geological conditions of Shimensi tungsten-polymetallic deposit in north Jiangxi province. Contributions Geol. Miner. Resour. Res. 27, 143–155 [in Chinese with English abstract]. doi: 10.6053/j.issn.1001-1412.2012.02.002.

Xiang, X.K., Wang, P., Sun, D.M., Zhong, B., 2013a. Isotopic geochemical characteristics of the Shimensi tungsten-polymetallic deposit in northern Jiangxi Province. Acta Geosci. Sin. 34, 263–271 [in Chinese with English abstract]. doi: 10.3975/cagsb.2013.03.02.

Xiang, X.K., Wang, P., Sun, D.M., Zhong, B., 2013b. Re-Os isotopic age of molybdenite from the Shimensi tungsten polymetallic deposit in northern Jiangxi province and its geological implications. Geology Bull. China 32, 1824–1831. https://doi.org/10.3969/j.issn.1671-2552.2013.11.015.

Xiang, X.K., Wang, P., Zhan, G.N., Sun, D.M., Zhong, B., Qian, Z.Y., Tan, R., 2013c. Geological characteristics of Shimensi tungsten polymetallic deposit in northern Jiangxi Province: Mineral Depos. 32, 1171–1187 [in Chinese with English abstract]. doi: 10.3969/j.issn.0258-7106.2013.06.006.

Xiang, X.K., Yin, Q.Q., Feng, C.Y., Wang, H., Liu, N.Q., Yu, Z.D., 2015a. Elements and fluids migration regularity of granodiorite alteration zones in the Shimensi tungsten polymetallic deposit in northern Jiangxi and their constrain on mineralization. Acta Geol. Sin. 89, 1273–1287. https://doi.org/10.3969/j.issn.0001-5717.2015.07.010 [in Chinese with English abstract].

Xiang, X.K., Yin, Q.Q., Sun, K.K., Chen, B., 2015b. Origin of the Dahutang syn-collisional granite-porphyry in the middle segment of the Jiangnan orogen: zircon U-Pb

geochronologic, geochemical and Nd-Hf isotopic constraints. Acta Petrol. Mineral. 34, 3–22 [in Chinese with English abstract]. doi: 10.3969/j.issn.1000-6524.2015.05.001.

Xiang, X.K., Yin, Q.Q., Zhan, G.N., Qu, K., Liu, X., Tan, R., Zhong, B., 2017. Metallogenic conditions and ore-prospecting of Shimensi tungsten ore section in the north of Dahutang area in Jiangxi province. Jilin Univ. (earth Sci. Ed.), 47, 645–658. https://doi.org/10.13278/j.cnki.jjuese.201703101 [in Chinese with English abstract].

Xing, S.J., Chen, D.S., Li, G.L., 2010. Analysis of the vertical distribution in the Zhangdongkeng W-Mo deposit of Jiangxi. China Tungsten Ind 25, 8–12. https://doi.org/10.3969/j.issn.1009-0622.2010.05.002.

Xue, H.M., 2021. Geochronology, geochemistry and stratospheric interactions of Late Mesozoic granitoids near the boundary between Anhui and Zhejiang provinces in the eastern segment of the Jiangnan orogenic belt. Acta Petrol. Sin. 37 (2), 433–461. https://doi.org/10.18654/1000-0569/2021.02.07.

Yang, J., Kang, L., Peng, J., Zhong, H., Gao, J., Liu, L., 2018. In-situ elemental and isotopic compositions of apatite and zircon from the Shuikoushan and Xihuashan granitic plutons: implication for Jurassic granitoid-related Cu-Pb-Zn and W mineralization in the Nanling Range. South China. Ore Geol. Rev. 93, 82–403. https://doi.org/10.1016/j.oregeorev.2017.12.023.

Yao, J., Shu, L., Santosh, M., Zhao, G., 2014. Neoproterozoic arc-related mafic-ultramafic rocks and syn-collision granite from the western segment of the Jiangnan orogen, South China: constraints on the Neoproterozoic assembly of the Yangtze and Cathaysia blocks. Precambrian Res. 243, 39–62. https://doi.org/10.1016/j.precamres.2013.12.027.

Ye, S.Z., Xia, J.H., Chen, W.H., Wang, G.H., 2016. Geological characteristics of Kunshan W-Mo-Cu deposit in Jiuling metallogenic belt in northern Jiangxi. China Tungs. Ind. 31, 7–13 [in Chinese with English abstract]. doi: 10.3969/j.issn.1009-0622.2016.04.002.

Yin, Q.Q., Xiang, X.K., Yu, Z.D., Yang, X.F., Wang, T.C., Zhong, B., Tan, R., Liao, J.H., Zhu, Y.S., 2020. Genesis of S-type Granites in the Pengshan Sn-polymetallic Ore Field, Northern Jiangxi Province and its Implications. Acta Geol. Sin. - Engl. Ed. 94, 1860–1873. https://doi.org/10.1111/1755-6724.14599.

Yin, Q.Q., Tang, J.X., Xiang, X.K., Zhao, X.Y., Wang, F.Y., Xu, Y.M., Guo, H., Yu, Z.D., Xie, J.L., Dai, J.J., Peng, B., 2024. Petrogenesis of reductive S-type granites from Pengshan district, northern Jiangxi province and their implications for Sn enrichment: evidence from in situ zircon LA-ICP-MS geochemistry. Earth Sci. Front. 31, 133–149 [in Chinese with English abstract]. doi: 10.13745/j.esf.sf.2023.9.3.

Yu, Z.D., Tan, R., Xiang, X.K., Xu, X.Y., Wang, T.C., 2021. Lead isotopic characteristics of Shimensi "multi-position in one" tungsten copper deposit in northern Jiangxi. China Tungs. Ind 36, 9–21. https://doi.org/10.3969/j.issn.1009-0622.2021.06.002.

Zartman, R.E., Doe, B.R., 1981. Plumbotectonics-the model. Tectonophysics 75, 135–162. https://doi.org/10.1016/0040-1951(81)90213-4.

Zhang, C., Sun, W., Wang, J., Zhang, L., Sun, S., Wu, K., 2017. Oxygen fugacity and porphyry mineralization: a zircon perspective of Dexing porphyry Cu deposit. China. Geochimica Cosmochim. Acta 206, 343–363. https://doi.org/10.1016/j.gca.2017.03.013.

Zhang, D.C., Mu, Z.G., Huang, F.S., Chen, C.Y., Zheng, S.H., 1984. Stable isotope studies of the Yanchuling tungsten-molybdenum ore deposit. Jiangxi Province. Mineral Depos. 02, 49–58 [in Chinese with English abstract].

Zhang, H.X., Sun, D.Z., Zhu, B.Q., Tu, X.L., 2000. Pb-Nd isotopic study of Proterozoic metamorphic sediments in north Jiangxi and its tectonic significance. Geology Bull. China 19, 66–71. https://doi.org/10.3969/j.issn.1671-2552.2000.01.011.

Zhang, M.Y., Feng, C.Y., Li, D.X., Wang, H., Zhou, J.H., Ye, S.Z., Wang, G.H., 2016. Geochronological study of the Kunshan W-Mo-Cu deposit in the Dahutang area, northern Jiangxi Province and its geological significance. Geotectonica Metallogenia 40, 503–516. https://doi.org/10.16539/j.ddgzyckx.2016.03.008.

Zhang, M.Y., Feng, C.Y., Li, D.X., Wang, H., Zhou, J.H., Ye, S.Z., Wang, G.H., 2018a. Geochemical and Hf isotopes of granites in the Kunshan W-Mo-Cu deposit, northern Jiangxi province: Acta Geol. Sin. 92, 77–93 [in Chinese with English abstract]. doi: 10.3969/j.issn.0001-5717.2018.01.006.

Zhang, M.Y., Feng, C.Y., Wu, G., Wang, H., Wu, Y., Han, M.M., Wu, W.H., 2018b. Fluid inclusion study and stable isotope characteristics of the Kunshan W-Mo-Cu deposit in the Dahutang area, northern Jiangxi Province. China. Acta Petrol. Sin. 34, 2615–2631.

Zhang, S., Chen, G.W., 2015. Gaseous transport and magmatic-hydrothermal mineralization of tungsten: Experimental study and its metallogenic implications. Chinese Journ. Geol. 50, 898–910 [in Chinese with English abstract]. doi: 10.3969/j.issn.0563-5020.2015.03.015.

Zhang, Z.H., Zhang, D., Wu, G.G., Luo, P., Chen, X.H., Di, Y.J., Lu, L.J., 2013. Re-Os isotopic age of molybdenite from the Meizikeng molybdenite deposit in northern Jiangxi province and its geological significance. Jilin Univ. (earth Sci. Ed.) 43, 1851–1863 [in Chinese with English abstract].

Zhang, Z.H., 2014. Research on metallization of the Dahutang tungsten multi-metal field, Jiangxi province, China [PhD thesis]. Beijing, China University of Geosciences Beijing 186p [in Chinese with English abstract].

Zhou, M.F., Yan, D., Kennedy, A.K., Li, Y., Ding, J., 2002. SHRIMP U-Pb zircon geochronological and geochemical evidence for Neoproterozoic arc-magmatism along the western margin of the Yangtze block. South China. Earth Planet. Sci. Lett. 196, 51–67. https://doi.org/10.1016/s0012-821x(01)00595-7.

Zhu, K.J., Fan, H.R., 1991. Geological and geochemical evidence for strata bound genesis of Jinshan gold deposit in Jiangxi province. Contributions Geol. Miner. Resour. Res. 6, 18–27 [in Chinese with English abstract].

Zou, X., Qin, K., Han, X., Li, G., Evans, N.J., Li, Z., Yang, W., 2019. Insight into zircon REE oxy-barometers: a lattice strain model perspective. Earth Planet. Sci. Lett. 506, 87–96. https://doi.org/10.1016/j.epsl.2018.10.031.